Powder Technology 398 (2022) 117130

Contents lists available at ScienceDirect

Powder Technology

journal homepage: www.elsevier.com/locate/powtec

Pore-scale simulation of fine particles migration in porous media using coupled CFD-DEM

Ahmed Elrahmani [a], Riyadh I. Al-Raoush [b,*], Hamza Abugazia [c], Thomas Seers [d]

[a] Environmental Engineering Masters Program, Qatar University, Doha, Qatar
[b] Department of Civil and Architectural Engineering, Qatar University, Doha, Qatar
[c] Department of Computer Science and Engineering, Qatar University, Doha, Qatar
[d] Department of Petroleum Engineering, Texas A&M University at Qatar, Doha, Qatar

ARTICLE INFO

Article history:
Received 12 August 2021
Received in revised form 8 November 2021
Accepted 10 January 2022
Available online 19 January 2022

Keywords:
Fine particles
Porous media
Pore scale
Computational fluid dynamics
Discrete element method
Parallel model
Microfluidic

ABSTRACT

Transport of fine particles in porous media has attracted a considerable interest over the past several decades given its importance to many industrial and natural processes. In order to control fine particles transport in porous media, the behavior itself needs to be predicted and analyzed. Which could be quite costly to do in a laboratory experiment, hence the modelling of such a behavior would be an optimum way to study. In this work, we present a coupled computational fluid dynamics-discrete element method (CFD-DEM) based modelling framework that is capable of simulating the migration of a large number of fine particles, on the colloids size through physically realistic porous media. The model was parallelized using Message Passing Interface (MPI) protocol to resolve particle-particle and particle-grain interactions for a large number of fine particles. The model's geometry was generated from computed tomography images of sand packs, the CFD solver were set to solve the fluid flow while the DEM were to solve the particles physical interactions. Immersed Boundary Method (IBM) were used to couple the two solvers in a resolved manner. The model's setup was first validated to capture single phase fluid flow behavior and then the coupling of the fluid flow and particle interaction was compared to experimental results. In order to validate the coupled CFD-DEM model, velocity profiles of fine particles, their diffusion in the pore space and the percentage of fine particles retained in the pore space obtained from micromodel experiment were compared to values obtained from simulations using the same pore space geometry and initial experimental conditions. The presented framework was shown to capture the bulk dynamics of fine particulate transport and deposition within geologically realistic and complex flow domains while minimizing execution time.

The model was used to study the impact of flow velocity and size of fines on permeability reduction of porous media due to migration of fine particles. Simulations indicate that permeability reduction due to fine migration in porous media is directly proportional to flow velocity. The time required to develop bridging and subsequent clogging of the pore space that lead to permeability reduction decreases as the flow velocity increases. The size of the fine particles has a significant impact on permeability reduction where the reduction in permeability increases as the size of particles increases. A faster and larger reduction in permeability was observed when a suspension of polydisperse particles was injected as opposed to a monodisperse suspension.

© 2022 The Authors. Published by Elsevier B.V. This is an open access article under the CC BY license (http://creativecommons.org/licenses/by/4.0/).

1. Introduction

Over the past several decades, phenomena related to the fate and transport of fine particles in porous media have gained increasing attention, owing to their importance within a variety of natural and industrial processes [1–6]. For instance, the presence of authigenic and detrital clays within clastic reservoirs can have a profound impact on reservoir performance during water flood operations [7,8]. In such settings, changes in the ambient physico-chemical regime within the pore environment caused by injected water can promote the mobilization of fines, with their subsequent entrapment within the pore throats of the reservoir framework, potentially leading to a several fold decrease in permeability and significant reduction in oil production [7,9–13]. Similarly, the migration of fine particles during proposed methane extraction by depressurization from gas-hydrate sediments could also potentially cause pore-throat clogging, dependent upon the topology and the geometry of the porous media. Thus, in order to predict the performance of tentative gas hydrate reservoirs, it is essential to

* Corresponding author.
E-mail addresses: ae1304061@qu.edu.qa (A. Elrahmani), riyadh@qu.edu.qa (R.I. Al-Raoush), ha1518096@qu.edu.qa (H. Abugazia), thomas.seers@qatar.tamu.edu (T. Seers).

https://doi.org/10.1016/j.powtec.2022.117130
0032-5910/© 2022 The Authors. Published by Elsevier B.V. This is an open access article under the CC BY license (http://creativecommons.org/licenses/by/4.0/).

understand the role of fines migration in gas hydrate sediments [14–16]. In addition to reservoir-scale effects, the dispersal of fines can also lead to irreversible formation damage in the near wellbore region, whereby the infiltration of water based drilling muds (typically clays with natural or synthetic weighting agents) or drilled solids can form a localized zone of reduced permeability and diminish well productivity [17].

Fine particle migration can also result in the modification of the hydro-mechanical properties in soil substrates which in turn promote soil erosion and reduce slope stability, potentially resulting in mass movement that lead to failure of civil engineering infrastructures such as earth dams and road embankments [18–20]. Infiltration of fine particles within unsaturated soils through downward vertical migration of subsurface systems creates pore pressure gradients and hence loss of cohesivity and mechanical competence of the soil matrix [21]. The flow of such fine particles induce internal erosion which can lead to a catastrophic slope failures [22]. In addition to altering the hydro-mechanical properties of soil substrates, mobile fine particulate, such as clays and colloids act as carrier agents which facilitate the dispersal of contaminants through groundwater by the adsorption and stabilization of organic and inorganic contaminants on their outer surfaces [23–25]. Moreover, in addition to the natural systems described above, analogous porous media are commonly used in industrial applications, such as the filtration of water and wastewater, where understanding of transport and entrapment dynamics of fine particles is critical to minimize clogging and hence enhance the efficiency of filter beds [26–28].

Motivated by the wide range of applications related to fine transport dynamics in porous media, researchers have focused on developing models that describe and predict the migration of fine particles in porous media at the fundamental constitutive scale (i.e., the pore-scale). Hirabayashi et al. (2012) used a two-phase Lattice-Boltzmann Method (LBM) to investigate the impact of size distribution of fines on permeability reduction in idealized porous media [29]. Whilst such studies provide valuable insights into the relationship between the size and concentration of fines on permeability reduction, the use of monodispersed spheres to represent the porous media limits accurate prediction of the underling dynamics of fines that take place in natural systems. Boccardo, Marchisio, and Sethi (2014) used micro-scale computational fluid dynamics (CFD) simulations based on colloid filtration theory to simulate deposition of fine particle in porous media having different pore space geometry and topology [30]. While such studies are important as they are capable of handling realistic pore geometries, however, the use of two-dimensional representation and exclusion of particle-particle interactions in the model, limits the applicability to real 3D systems where particle interactions are significant. Li and Prigiobbe (2018) as well as K. Zhou et al. (2018) used a Lattice-Boltzmann - Discrete Element Method (DEM) based modelling framework, coupled with Immersed Boundary Method (IBM) to understand the fundamental transport behavior of poly-disperse fine particles and their impact on fluid flow in porous media [31,32]. J. Su et al. (2019) adopted the Efficient spheRical partIcle and Geometry Interaction Detection (ERIGID) algorithm for a coupled CFD-DEM framework to study fluid-particle-flow concentrations and pore-throat clogging mechanisms [33]. Whilst capable of handling arbitrary geometries and particle-to-particle and particle-to-wall interactions, the three latterly discussed models [31–33] were limited by the comparatively diminutive number of simulated particles that could be simultaneously represented. Furthermore, similar to [30], the representation of the modelling domain was limited to two dimensions, which does not comprehensively capture the behavior of the clogging in real porous media, and assumes cylindrical fine particles extruded perpendicular to long and medial axes of the model domain [31–33]. With the exception of [33] who performed a separate validation of the CFD solver and a discrete particle's terminal settling velocity, validation methods for the aforementioned studies are generally limited. Importantly, in the work discussed above there are no attempts to validate numerical simulations against experimental results that capture the full flow field behavior of the modelled porous media and its mobilized fine fraction.

While the CFD-DEM framework was implemented and used for different applications, the use of the CFD-DEM framework to simulate a large number of fine particles on the order of colloids size through physically realistic porous media was not approached in previous studies. This is mainly due to limitations related to the use of idealized geometry to represent the porous media and the limitations of resolving fine-grains interactions on a resolved scheme which in turn limited the number and size of particles being used in the simulations in previous studies.

In this work, we present a numerical setup of a coupled CFD-DEM modelling framework capable of simulating the migration of a large number of fine particles on the colloids size in realistic pore geometries with non-spherical grains. The model was parallelized using MPI to resolve particle-particle and particle-grain interactions in order to simulate a large number of fine particles within the pore-space. Physically realistic geometry of porous media obtained from computed tomography images of sand packs was used in the model. The model's setup was validated by benchmarking single phase finite volume simulations using an idealized domain (i.e., single cylinder) and by comparing its results to a micromodel experiment using the exact geometry. Comparison between the simulation and micromodel experiments was performed using a novel image processing workflow executed using OpenCV which allowed tracking and characterization the behavior of the mobile particles over the duration of the micromodel experiment.

The structure of the paper is as follows, implementation details of the coupled CFD-DEM modelling framework as well as the parallelization scheme are presented in Section 2. Validation of the model using micromodel experiment is presented in Section 3. Applications of the model are presented in Section 4.

2. Numerical model structure

2.1. Overview of the model

In this section, a general description of the main capabilities of the model is outlined. More details will be discussed in subsequent sections.

2.1.1. Simulation of small fines sizes

Simulation of small particles, on the order of colloids, is considered a challenge. In order to resolve fluid-fines interactions using resolved Immersed Boundary Method (IBM), the size of particles must be larger than the size of mesh elements of the fluid domain. However, reduction of sizes of mesh element of the fluid domain generates a high Courant Number that yields a poor capture of the flow behavior at the scale of mesh size. Alternatively, reducing the CFD solver's time step leads to a high computational cost. In this work, two approaches were used to overcome the challenge of simulating small particle size. In the first approach, sizes of fine particles that covers the mesh elements, of the fluid domain, were increased dynamically while their volume was maintained constant during the IBM computations. More details about this step are given in Section 2.3.1. In the second approach, the coupling interval, which is the number of DEM steps executed before fine particles data is transferred to the CFD solver, was dynamically optimized to lower the computational cost while maintaining an accurate calculation for fluid-fines interactions. More details are given in Section 2.2.2. Moreover, to implement and optimize computational efficiency, the model was parallelized by distributing the computations of its domain among the cores of machine used in the simulations. More details will be discussed in Section 2.5.

2.1.2. Simulation of fines in a complex geometry of porous media

Simulation of fluid flow with fine migration in a complex pore space requires considering two types of mesh cells, namely the mesh cells that are completely occupied by the solid phase of the porous media

(i.e., grains) and the cells that are occupied by boundaries of grains. In order to takes into account fluid-solid and fluid-fines interactions, a resolved IBM scheme needs to be implemented which can be a real challenge due to the complexity of the domain and the demand for high computational cost. In the model that we present in this work, we implemented an adoptive dynamic scheme that eliminates mesh elements that are completely occupied by the grain particles for a better mesh resolution. Moreover, mesh elements that are partially occupied by grains were adjusted by generating hexahedral mesh representation that preserve the geometry of the solid phase and therefore the interactions with fluids and grains. More details will be presented in Section 2.4.

2.1.3. Simulation of a large number (i.e., concentration) of fine particles

Simulating a large number of fine particles is not a trivial task given the fine-fine separation distance that needs to be identified in the model to distinguish between fine-fine and fine-grain interactions. In this work, we implemented a dynamic fines-neighbors-list updating scheme that is updated at certain time-steps for mobile particles to avoid redundancy of fines-neighbors-list of stationary particles. Additionally, in order to accurately and efficiently model fine-grain interactions, a physically-realistic model of elasticity was implemented for fines and grains to reduce the time-step need to capture a resolved interactions. More details will be presented in Section 2.2.2.

2.2. Mathematical model

2.2.1. Fluid flow equations

The fluid flow model was computed using the finite volume method, where the fluid domain was represented by small control volumes in which the mass and momentum of the fluid were computed [34,35]. Determination of the field mass and momentum was achieved by integrating the governing equations over the domain cells. The CFD open-source toolbox OpenFOAM solves the coupled Navier-Stokes equations [Eq. (1a)] and the continuity equation [Eq. (1b)] for incompressible fluid to compute the pressure p and velocity u [36].

$$\frac{\partial}{\partial t}(\rho u) + \nabla\cdot(\rho u u) = \nabla p + \left[\nabla\cdot\left(\mu\left(\nabla u + \nabla u^{T}\right)\right)\right] + F_{sa} \tag{1.a}$$

$$\nabla\cdot u = 0 \tag{1.b}$$

Where ρ is the fluid density, μ is the dynamic viscosity and F_{sa} is the net external force exerted on the fluid body. Fig. 1 shows the boundary conditions for pressure and velocity. The flow was modelled as pressure-driven, hence pressure values at both the inlet and outlet were constant, whilst the velocity was calculated. The other two sides are considered symmetrical, whereby the velocity is considered with a slip-condition. Conversely, the mesh boundary representing the interface between the grain particles and the fluid domain has a no-slip velocity condition. This ensures that the velocity at the surface of the framework is zero.

2.2.2. Equations governing particle interactions

Discrete Element Method (DEM) is a Lagrangian approach for calculating the trajectory of each particle in a large granular system [37]. The particle trajectory is computed by considering the interactions between other particles/walls and how they influence the particles' behavior. Particle motion is governed by translation and rotational changes. Newton's laws for translation and rotational motion are derived from the following equations for each particle i [Eqs. (2a) & (2b)].

$$m_i\frac{dv_i}{dt} = m_i g + \sum_{N_p} F_i^{p-p} + \sum_{N_w} F_i^{w-p} + F_i^{f-p} \tag{2.a}$$

$$I_i\frac{d\omega_i}{dt} = \sum_{N_p} r_{ic}\times F_i^{p-p} + \sum_{N_w} r_{ic}\times F_i^{w-p} + T_i^{f-p} \tag{2.b}$$

Where m_i is the particle mass, v_i is the velocity, g is the gravitational acceleration and N_p and N_w are the numbers of particles and walls respectively. F_i^{p-p}, $F_i^{w-p}$and F_i^{f-p} are the forces applied from the other particles, walls, and fluid, respectively, on the i^{th} particle. For the torque equation, I_i is the particle inertia, ω_i is the angular velocity and r_{ic} is the torque radius. The force acting on the particle i from a secondary particle j is calculated based on the granular hertz model, as two components (normal and tangential: Fig. 2) [38–43]. The normal force [Eq. (3a)] is calculated by two terms: the first term represents the spring force, which depends on the normal overlap δn_{ij},and the second term describes the damping force, which depends on the

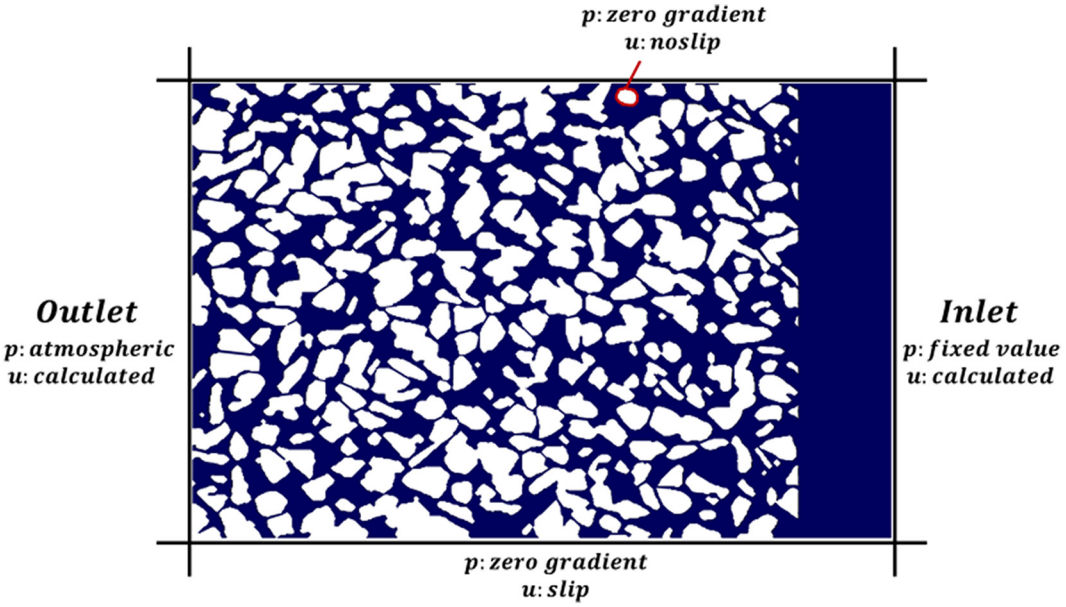

Fig. 1. Boundary conditions of pressure and velocity for the fluid domain.

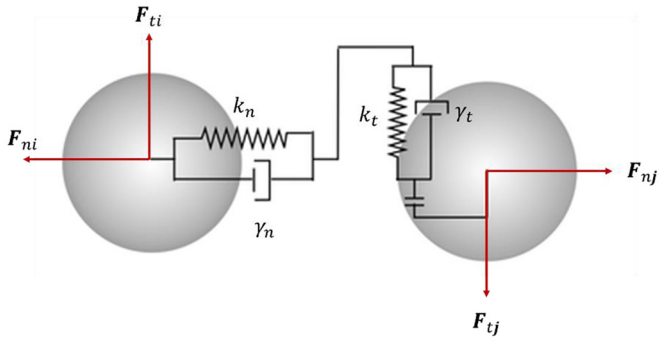

Fig. 2. Illustration for the particle interactions model used in the DEM solver (Granular Model Hertz [40]).

normal relative velocity vn_{ij}. The tangential force [Eq. (3b)] also consists of two components: the shear force, which depends on the tangential overlap δt_{ij},and the damping force, which depends on the tangential relative velocity vt_{ij}.

$$F_n = k_n \delta n_{ij} - \gamma_n v n_{ij} \tag{3.a}$$

$$F_t = k_t \delta t_{ij} - \gamma_t v t_{ij} \tag{3.b}$$

The shear force between the particles in contact is considered in the calculation, by applying the 'history' command in the DEM solver, which induce tangent displacement between the particles. k_n and k_t in the equations represents the elastic constants for normal and tangential contact between the particles, while γ_n and γ_t are the isoelastic damping constant for normal and tangential contact respectively. The both coefficients k and γ are calculated based on the material properties defined for the particles, such as Young's and the shear modulus, Poisson ratio, and the coefficient of restitution. The same model is used to calculate the interactions between fine and grain particles.

2.2.3. Coupling scheme equations

The CFD-DEM coupling scheme utilizes a four-way coupling model, where fluid-particle and particle-particle interactions are taken into account. The coupling approach is a Eulerian-Lagrangian method, which accounts for the granular phase by introducing a volume fraction α_l into Navier-Stokes equations [Eq. (4)] [37,44].

$$\frac{\partial}{\partial t}(\alpha_l \rho_l u) + \nabla\cdot(\alpha_l \rho_l u u) = -\nabla p - K_{sl}(u-v) - F_{s-l} + \nabla\tau + \alpha_l \rho_l g \tag{4.a}$$

$$\nabla\cdot(\alpha_l u) = 0 \tag{4.b}$$

$$K_{sl} = \frac{\alpha_l \left|\sum F\right|}{\forall_{cell}|u-v|} \tag{4.c}$$

$$F_{s-l} = \frac{(F_{drag} + F_{Archim})}{\alpha_l} - \alpha_l \forall_l g \tag{4.d}$$

Where τ represents the viscous shear stress tensor and K_{sl} is the implicit momentum source term, $\forall_l$ and $\forall_{cell}$ are the fluid and the cell volumes respectively. The drag force acting on each particle was calculated in a resolved manner using the method proposed by Shirgaonkar et al. (2009) [45]. In the resolved surface model the fluid flow surrounding each particle can be obtained. This method typically requires a high computational cost. However, in this work, this was overcame by parallelizing the model. Whereas the volumetric buoyancy force was calculated from the density difference between fluid and particles. The coupled mathematical scheme is presented in Fig. 3.

2.3. Numerical setup

2.3.1. Numerical solvers

First-time derivatives of parameters were calculated using the Euler discretization scheme, which uses the current time and previous time to evaluate the derivative as described in [Eq. (5)] for any parameter ϕ.

$$\frac{\partial}{\partial t}(\phi) = \frac{\phi - \phi_o}{\Delta t} \tag{5}$$

Linear interpolation was used to evaluate mesh face values, which was achieved by averaging the cell center values of cells on either side of the surface by assuming parameters change linearly between neighboring cell centers [Eq. (6)].

$$\phi_f = 0.5(\phi_c + \phi_d) \tag{6}$$

The divergence for the velocity and the viscous stress-tensor term in the fluid momentum equation was evaluated using Gauss theorem with linear interpolation. The divergence for mass flux was also done using the Gauss theorem, but the Linear-Upwind Stabilized Transport interpolation scheme was used instead, as it is has shown greater stability. Additionally, for the calculation of the surface normal gradient, the scheme was uncorrected since the mesh is exclusively hexahedral [46]. The Laplacian term of the fluid equation was solved using Gaussian integration with linear interpolation which is first-order accurate and bounded. Cell gradients were evaluated using the Gauss theorem which solves the volume integral as a surface integral [Eq. (7)].

$$\int V(\nabla \cdot u)dV = \oint S(n \cdot u)dS \tag{7}$$

The primary solver for single phase fluid flow used herein was the Pressure Implicit with Splitting of Operators (PISO) algorithm, which is an extension of the Semi-Implicit Method for Pressure Linked Equations (SIMPLE) algorithm [47–50]. It operates based on a series of predictors and correctors until convergence. PISO starts by guessing the initial values for pressures and velocities and progresses through a series of correctors to update their values. The algorithm was set to repeats the prediction and correction steps until convergence to the given tolerance ($T = 10^{-6}$). To explain the algorithm, the one-dimensional momentum equation for the fluid, ignoring the gravity effect, [Eq. (8)] is solved as an example using the PISO algorithm.

$$\frac{\partial u}{\partial t} + \frac{\partial}{\partial x}(uu) = \frac{\partial p}{\partial x} \tag{8}$$

The predictor equation [Eq. (9a)] discretizes the original equation using the schemes discussed previously, where the predicted values are denoted by *. In solution vector form [Eq. (9b)], C is the coefficient array forming the multiplicand to the solution vector u^*, with r being the right-hand side explicit source term omitting the pressure gradient. The matrix C is split into its diagonal matrix A and its off-diagonal matrix H',as shown in [Eq. (9c)], which is solved to obtain the predicted fluid velocity.

$$\left[\frac{1}{\Delta t} + \left(\frac{u^n_{i+\frac{1}{2}} - u^n_{i-\frac{1}{2}}}{2\Delta x}\right)\right]u^*_i + \left(\frac{u^n_{i+\frac{1}{2}}}{2\Delta x}\right)u^*_{i+1} - \left(\frac{u^n_{i-\frac{1}{2}}}{2\Delta x}\right)u^*_{i-1} = \frac{u^n_i}{\Delta t} - \left(\frac{\partial p}{\partial x}\right)\Big|^n_i \tag{9.a}$$

$$\boldsymbol{C u^*} = \boldsymbol{r} - \boldsymbol{\nabla p^n} \tag{9.b}$$

$$\boldsymbol{A u^*} + \boldsymbol{H' u^*} = \boldsymbol{r} - \boldsymbol{\nabla p^n} \tag{9.c}$$

The discretized explicit velocity corrector equation [Eq. (10a)] uses the predicted velocity and pressure values u^*, p^*,as well as the old

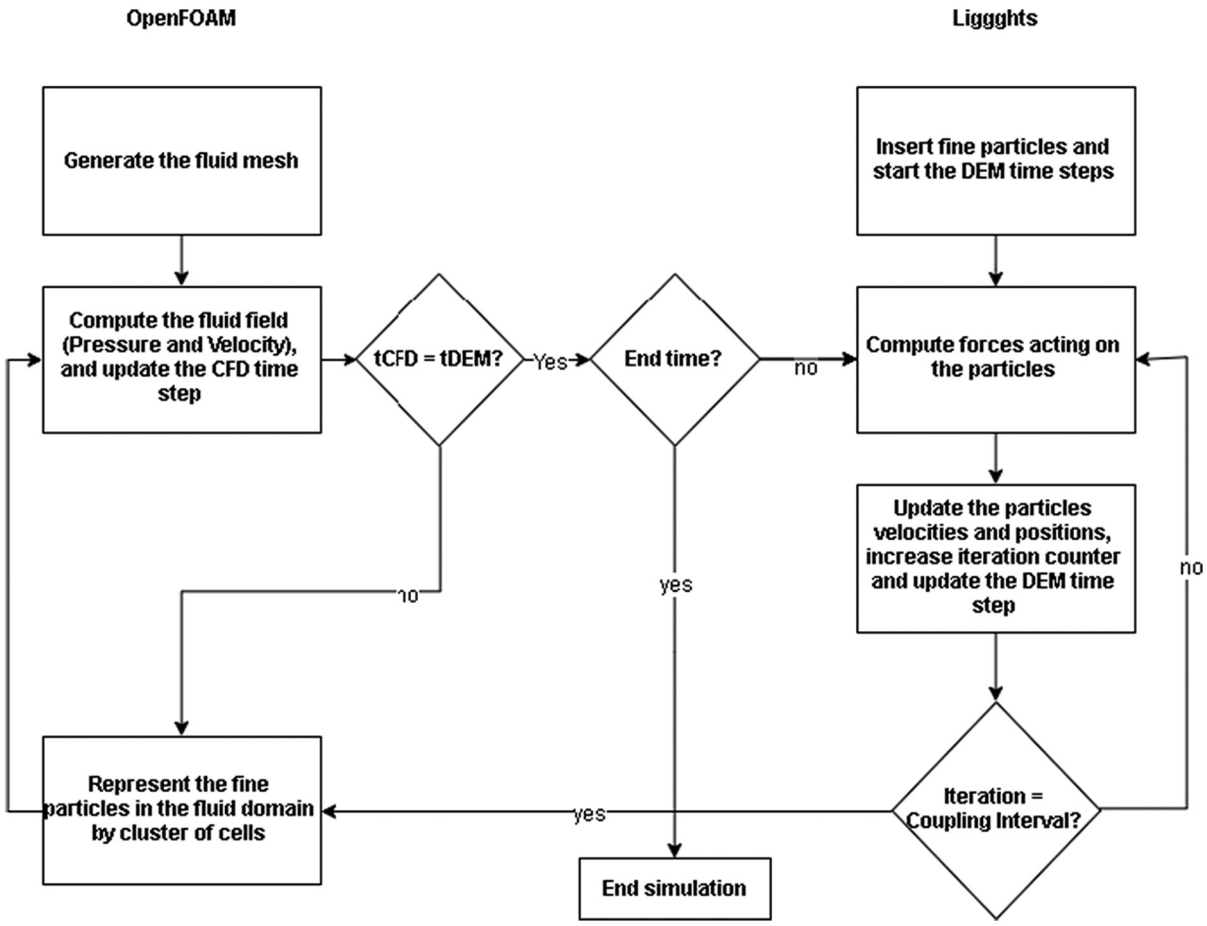

Fig. 3. The CFD-DEM coupled modelling algorithm used to predict the fine migration in porous media.

value of the velocity u^n to solve for the corrected velocity u^{**}, as shown in [Eq. (10b)]. The value of the velocity is calculated using the Preconditioned Bi-Conjugate Gradient (PBiCGStab) numerical solver, which has good parallel scaling [51,52]. While the pressure value is calculated using the Generalized Geometric-Algebraic Multi-Grid (GAMG) solver.

$$\left[\frac{1}{\Delta t}+\left(\frac{u^n_{i+\frac{1}{2}}-u^n_{i-\frac{1}{2}}}{2\Delta x}\right)\right]u^{**}_i+\left(\frac{u^n_{i+\frac{1}{2}}}{2\Delta x}\right)u^*_{i+1}-\left(\frac{u^n_{i-\frac{1}{2}}}{2\Delta x}\right)u^*_{i-1} = \frac{u^n_i}{\Delta t}-\left(\frac{\partial p}{\partial x}\right)^*_i \tag{10.a}$$

$$\boldsymbol{u}^{**}=\boldsymbol{A}^{-1}\boldsymbol{H}-\boldsymbol{A}^{-1}\nabla\boldsymbol{p}^* \tag{10.b}$$

Where;

$$\boldsymbol{H}=\boldsymbol{r}-\boldsymbol{A}^{-1}\boldsymbol{H}\prime \tag{10.c}$$

Geometric Agglomerated Algebraic Multigrid solver (GAMG) was used to calculate pressure, as well as the volumetric flux. The GAMG solver works by creating a coarse grid using different agglomeration and coarsening algorithms. These agglomeration algorithms can either be geometric, using the mesh geometry, or algebraic, by applying the same techniques to the matrix itself. The coarse grid was then used to create an initial solution for the fine grid [53]. The velocity and nuTilda were solved using Preconditioned Biconjugate Gradient Solver (BiCGSTAB), since it is a faster more smoothly converging variant of Bi-CG. It also uses a preconditioner to accelerate its convergence [51].

In this work, the Immersed Boundary Method (IBM) was used to account for the impact of flowing particles in the fluid domain. Peskin (1972) was the first to introduce IBM to simulate cardiac mechanics and its associated blood flow [54]. One of the advantages of using IBM is to facilitate grid generation, as the body does not have to conform to the cartesian grid explicitly. Another advantage is that the complexity of the domain geometry when simulating a non-boundary conforming Cartesian grid does not significantly affect the grid complexity and quality. Also, due to the stationary non-deforming Cartesian grid, IBM can deal with moving boundaries [55,56]. For simplicity, consider a rectangular field containing both the fluid region and the bond solid in Fig. 4. When IBM is used to solve fluid flow within the complex geometry, the resulting rectangular domain would consist of fluid regions, in which the fluid velocity is governed by Navier-Stokes equations, and solid regions have a velocity of zero. The marker function M(x) [Eq. (11)] is then used to adjust the flow velocity results in the equation below [Eq. (12)] [57].

$$M(x)=\begin{cases}1 \textit{ in the fluid}\\ 0 \textit{ in the solid}\end{cases} \tag{11}$$

$$u(x)=M(x)\,u(x)+(1-M(x))\,v(x) \tag{12}$$

For each time step, a particle's associated properties (position, velocity, angular velocity, force, etc.) in the DEM solver were calculated by using the previous time-step pressure field, as well as velocity. Then, considering the solid phase in the mesh, the Navier-Stokes equations were solved in the complete fluid domain where each particle is represented by a cluster of cells. The fluid velocity was calculated in the CFD

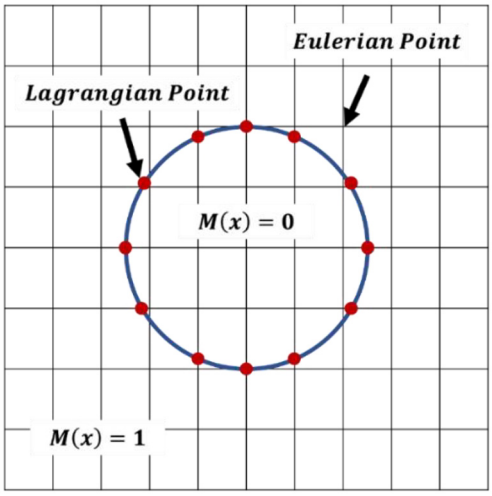

Fig. 4. Immersed Boundary Method (IBM) illustration for particle covering fluid cells.

solver along with the pressure, depending on the precise position of the particles. Finally, the velocity and pressure field correction of the fluid phase takes place using the particle's positional information. This process is repeated with every iteration until the simulation is complete [58,59]. The void fraction, which is used in the governing equations presented above, defines the space that particles occupy within a fluid cell. The void fraction field is placed in cells whose centers fall within the particle's body. One disadvantage of this model is that the particle should cover approximately eight cells to have accurate results. This was avoided by increasing the region in which the particles influence by scaling them up with a constant volume, for calculation of the void fraction [37].

2.3.2. Time step selection

The stability of the CFD model depends heavily on the time step choice. A reliable method of determining the appropriate time step is the use of the Local Courant number, shown in [Eq. (13)]

$$Co = \frac{|u_{cell}|\Delta t_{CFD}}{\Delta x} \tag{13}$$

Where Co is Courant number and Δx is the cell length. The timestep was set so that the courant number value does not exceed one; to ensure that the fluid does not travel a distance greater than the cell length per time step [46]. For the DEM time step choice, Δt_{DEM} must be small enough to capture a collision between two or more particles. Hertz criteria [Eq. (14)] was used to obtain a sufficient Δt_{DEM}.

$$\Delta t_{DEM} = 2.87\left(\frac{m_{eff}^2}{r_{eff}\, E_{eff}^2\, U_{max}}\right)^{0.2} \tag{14}$$

Where m_{eff}, r_{eff} and E_{eff} are the particle's effective mass, radius, and Young's Modulus respectively. The time for DEM simulations is typically about 10^{-7} and could reach lower values in the case of stiff materials with a high Young's Modulus [60], however, by reducing Young's Modulus, the DEM time step could be increased [46].

The coupling interval is the number of DEM time steps that run before sending the particle data to the CFD solver. Thus, a coupling interval of ten means that ten DEM iterations are calculated for each CFD iteration. The coupling interval CI was calculated as shown below [Eq. (15)]. CI should be always an integer that is higher than or equal to one, where Δt_{CFD} is at a maximum is equal to Δt_{DEM}.

$$CI = \frac{\Delta t_{DEM}}{\Delta t_{CFD}} \tag{15}$$

2.4. Geometric representation of porous media

3D Computed tomography images of sand packs were obtained at the Argonne National Laboratory (ANL) synchrotron facility [4]. 2D sections (orthoslices) were obtained from reconstructed volume images of these scans, which were subsequently binarized using global thresholding. A MATLAB code was used to extract boundaries of grain particles from the segmented images by establishing line segments where the gradient value between two adjacent pixels is non-zero, which were subsequently converted to polylines in AutoCAD. The process of generating polylines yielded a slight alteration of the geometry of the very small throats in the 2D image. A morphological operation (i.e., opening) was performed so that boundaries of grains and pore throats exactly match the raw 2D image (i.e., unsegmented) that was obtained from raw 3D computed tomography images. To create a 3D image that will be used in the simulation, 30 cross-sections (i.e., 2D image) were stacked in the vertical direction to create a 3D image (i.e., slab) that was used in the numerical simulation. This vectorized representation of the pore structure was tessellated to form a triangulated mesh amenable to DEM modelling. Additionally, the geometry was used to create the fluid domain mesh for the CFD component of the coupled model. Fig. 5 illustrates the geometry creation workflow described above.

The fluid domain mesh was created and enhanced using the built-in libraries in OpenFOAM. The features of the solid's geometry were extracted using the SurfaceFeatureExtract tool. This process involves simplifying the geometry by only including edges/features whose angles exceed a determined value for decimation. These abstracted features were used to create the hexahedral mesh-based representation of the fluid domain. This process starts by encompassing the entire domain with a background hexahedral mesh using BlockMesh, with further refinement used to fit the mesh the solid's geometry using SnappyHexMesh. This refinement procedure was performed at multiple levels to find an optimum balance between the minimization of the flow domain mesh size (and thus computational time), and the fidelity of the model representation the pore space geometry. The refinement process initializes at a specific vertex within the mesh, splitting the hexahedral background mesh elements to capture the details of framework edges, with cells that lie within manifold sub-regions representing the solid frame removed. The remaining cells' vertex points were then moved to snap to the framework's surfaces to eliminate stepped edges in order to ensure accurate representation of the fluid domain (Fig. 6).

2.5. Model parallelization

CFD and DEM models were both parallelized to achieve faster computation. Information was passed between processors using Message Passing Interface (MPI): a standardized inter-process communication protocol. The parameters of both particles approaching processor boundary and boundary mesh elements were passed between processors. Two different geometries were simulated multiple times using a different number of processors to find the optimal number of threads. The geometries used were taken from different image samples, both having dimensions of 6.7 mm by 5 mm and porosities of 0.503 (Fig. 7a) and 0.421 (Fig. 7b) respectively.

Throughout the simulations, the ideal number of processors required to optimize the computational time was the physical processors (cores) rather than the total number of hyper-threads, as shown in Fig. 8. This is mainly due to the fact that the processes are CPU-bound as opposed to I/O bound.

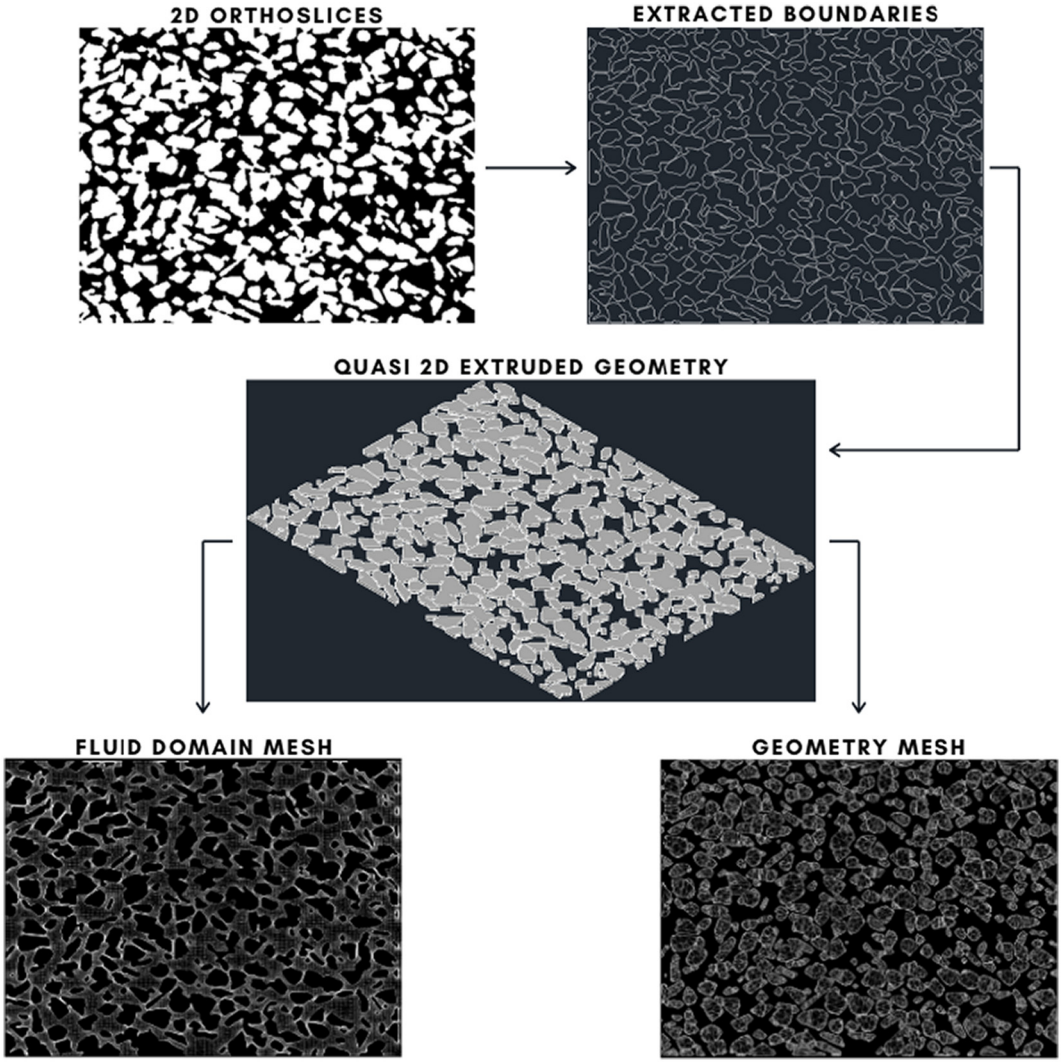

Fig. 5. Geometry creation from a pore-scale image for DEM and CFD meshes.

3. Validation of the model

The model's setup was first validated to capture single phase fluid flow behavior and then the coupling of the fluid flow and particle interaction was compared to experimental results for fines migration in porous media. In order to validate the coupled CFD-DEM model, velocity profiles of fine particles and their diffusion in the pore space obtained from the micromodel experiment were compared to values obtained from simulations using the same pore space geometry and initial experimental conditions. Moreover, an additional validation of the model's setup was conducted by comparing the percentage of fine particles retained in the pore space obtained from simulation and the micromodel experiment.

3.1. Micromodel experiment

A micromodel experiment was performed to validate the coupled numerical model and to verify that the CFD-DEM framework is capable of capturing the global behavior of fines migration within a substantial flow domain (i.e., consisting of tens of pore bodies) within complex and arbitrary pore geometries. The micromodel experiment was conducted using a borosilicate glass microfluidic chip supplied by Micronit Microfluidics BV, which has a sand pack-like geometry (Fig. 9c). The pore networks are etched into the glass substrate then fused with a plain glass wafer coverslip to form a quasi-two-dimensional pore network. The micromodel had a 20 μm channel depth and consisted of a 20 × 10 mm flow domain. The microfluidic channel surface area is hydrophilic, having an average contact angle of 20°. Micromodel permeability, porosity, and pore volume were 2.5 Darcy, 0.58, and 5.7 μL respectively. The fine particles used in the experiment were modified carboxylate polystyrene latex particles (MAGSPHERE INC) with a diameter of ~5 μm, and a density of ~1.05 g/cm^3. Ten percent volume of the uniform polystyrene latex particles were diluted with water to prepare to obtain a concentration of 2.9×10^7 colloids/mL which was the optimal concentration for injection into the micromodel avoiding inlet pore plugging. The diluted suspension was agitated for 15 min before each experiment and was sonicated using an ultrasonic processor (SONICS, Vibra cell) in a water bath for 30 min, in order to form a fine particulate suspension. The experimental setup used in this study is schematically shown in Fig. 9b. A microscope stage (Leica Z6 APO) was placed above the glass micromodel to view the behavior and interactions of the fine particles. A precision syringe pump (Kats Scientific, NE-1010) was connected to the inlet of the microchip to inject the fine particulate solution, while the outlet was open to atmospheric pressure. Note that a 2.75 × 2 mm area of the micromodel pore structure was captured using this imaging setup, which was used to validate the numerical model presented in the preceding section (see Fig. 9d). More detailed about the experiments can be found in [61,62].

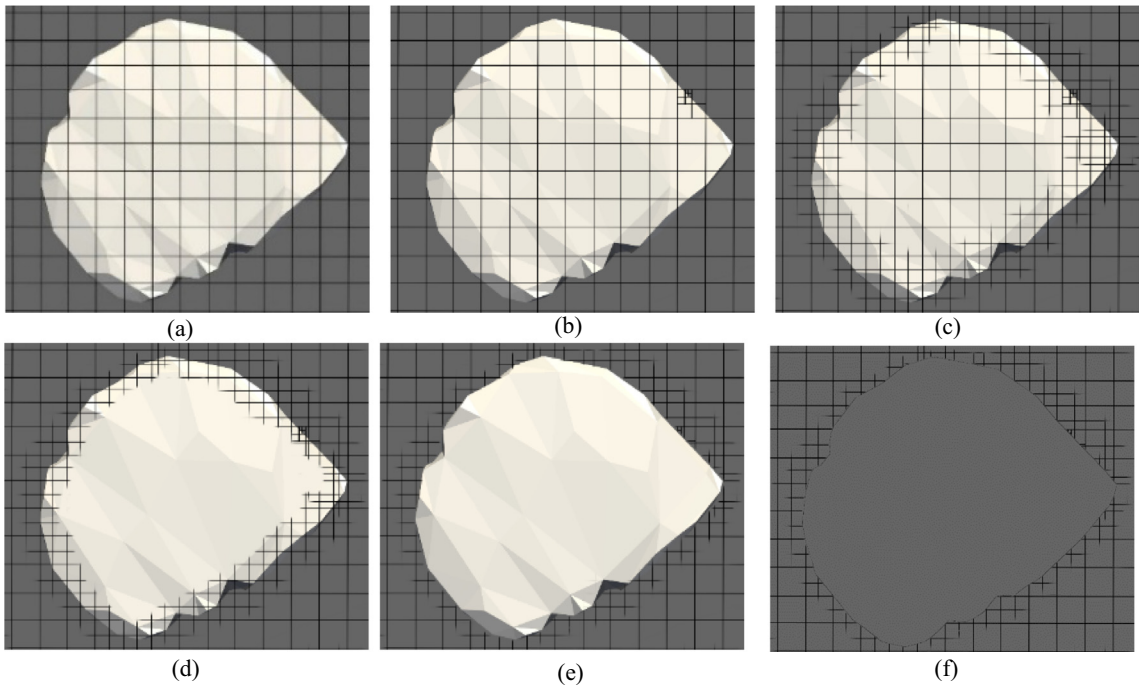

Fig. 6. Steps to create the mesh for the fluid domain using framework particles. (a) Encompassing the entire domain with a background mesh using BlockMesh. (b) and (c) Further refinement used to fit the mesh of the solid's geometry using SnappyHexMesh. (d) Cells that fall within manifold sub-regions representing the solid frame removed. (e) The remaining cells' vertex points are then moved to snap to the framework's surfaces. (f) Final mesh representing the fluid domain around the solid particles.

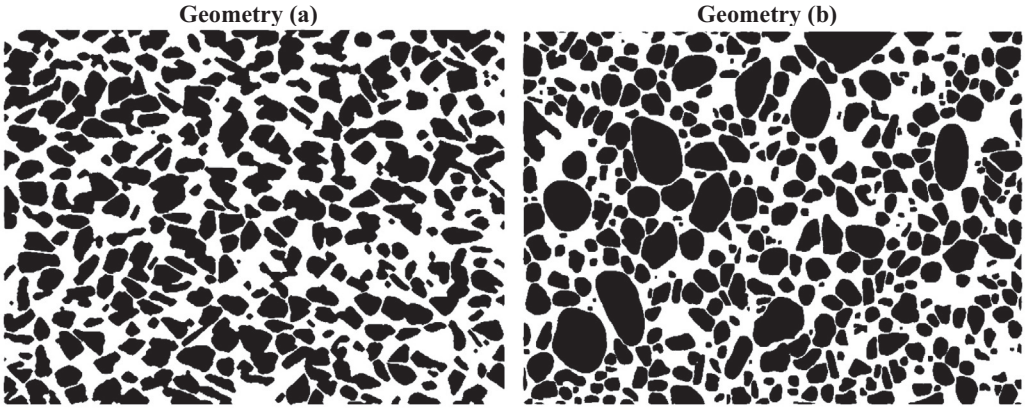

Fig. 7. Pore-scale geometries used in the simulations to find the optimum number of processors without increasing the communication overhead for the parallelization step.

Video footage was recorded continuously over course of the experiment to capture the transport dynamics of the fine particulate suspension. The video recordings were split into a sequence of consecutive standalone images, which were then processed using OpenCV: an open-source computer vision library [63]. Noise from the raw grayscale images was reduced using Gaussian smoothing and segmented using manual thresholding, with morphological operations (erosion and dilation) used to clean the binarized images [64]. Contours describing the shape of each fine particle's perimeter were extracted using OpenCV's findContours function. This is achieved by linking the edges of each isolated connected component representing discrete particles [63,64]. Contours were subsequently used to calculate the centroid coordinates of each particle. The steps of the image processing workflow are presented in Fig. 10. Even though the microchip was cleaned thoroughly after each experiment, many particles remained attached to the bottom of the micromodel where the fluid velocity was low [65]. To ensure accurate measurements on the particles of interest, these attached particles must be disregarded prior to the measurements. This was accomplished by detecting the particles that remained immobile over duration of the experiment.

The coordinates of the centroid of each particle mapped over consecutive images was used to approximate particle velocity by evaluating the associated displacement magnitude per time step. For a given particle, each successive position was identified by approximating candidate displacements in the following frame using an acceptance criterion (Fig. 11). The candidate position with the minimum linear and angular displacement was then selected out of prospective positions (Fig. 11a). By evaluating the displacement of each particle between frames, the velocity for each particle was calculated given the temporal resolution of the video sequence. Particle velocities for a single frame are illustrated in Fig. 11b, where the length of the leading arrow represents the displacement magnitude and trajectory of a given particle.

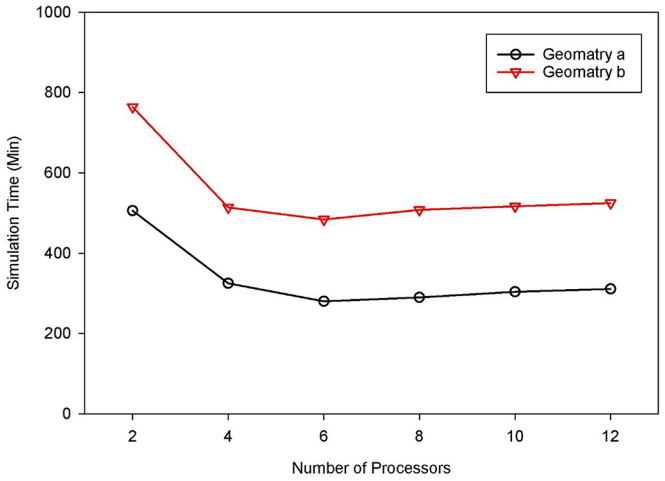

Fig. 8. Simulation time of the migration of 10,000 particles in geometries "a" and "b" at flow velocity of 0.042 cm/min using different number of threads using a six-core machine (Intel Xeon E-2276 M CPU and 125 RAM).

3.2. Validation of the CFD model setup

In fluid mechanics, fluid movement around a basic geometry, such as a cylinder, is a conventional problem, with numerous reported findings in the literature. The fluid domain used for initial validation of the CFD numerical setup was 50d × 63d × d,where d = 0.1 mm.with a 2d diameter cylinder placed 23d from the inlet face (Fig. 12). The setup validation entailed changing the Reynold's number R_e [Eq. (16)] and calculating the drag coefficient [Eq. (17)] from the model, with the obtained C_d compared to equivalent values established in the literature.

$$R_e = \frac{u\,d}{\nu} \tag{16}$$

$$C_d = \frac{2\,F_{drag}}{\rho_f\,d\,u^2} \tag{17}$$

Table 1 below presents a comparison between the mean drag coefficient for different Reynold's numbers for the proposed numerical model's setup and the results presented previously in the literature [66–69]. There is good agreement between the results; hence, the proposed model's setup is deemed reliable for the flow prediction around simple geometries.

The microfluidic chip designed by Micronit was used to validate flow behavior for more complex geometry. An image of the micromodel's flow domain was used to construct the benchmark model's geometry, which was scaled to equivalent dimensions. Validation of the model's setup was achieved by comparing the calculated permeability (k) of the benchmark model to the intrinsic permeability of the microfluidic device (Fig. 13).

Table 2 presents values of porosity and permeability obtained from the model compared to the chip specifications from the manufacturer, which shows good agreement. As a consequence, we conclude that the CFD setup is well suited towards simulating fluid flow in complex geometries. Moreover, the error between the results is not only based on CFD model's setup deficiencies but could also be related to inaccuracies in the geometric representation of the digitized and tessellated pore system. The etching technique used for the physical micromodel compared to the numerical model, along with the morphological operations undertaken during the image processing stage created dilated path flows by eroding the grain particles, which is expressed in the differential between the two reported porosities.

3.3. Validation of the coupled CFD-DEM

The validation of the coupled CFD-DEM model within flow domain comprised of a significant number of heterogeneous pores (i.e. tens of pore bodies) is a non-trivial undertaking but is critical towards confirming the ability of the presented modelling framework in capturing the transport dynamics of fines migration within geologically realistic

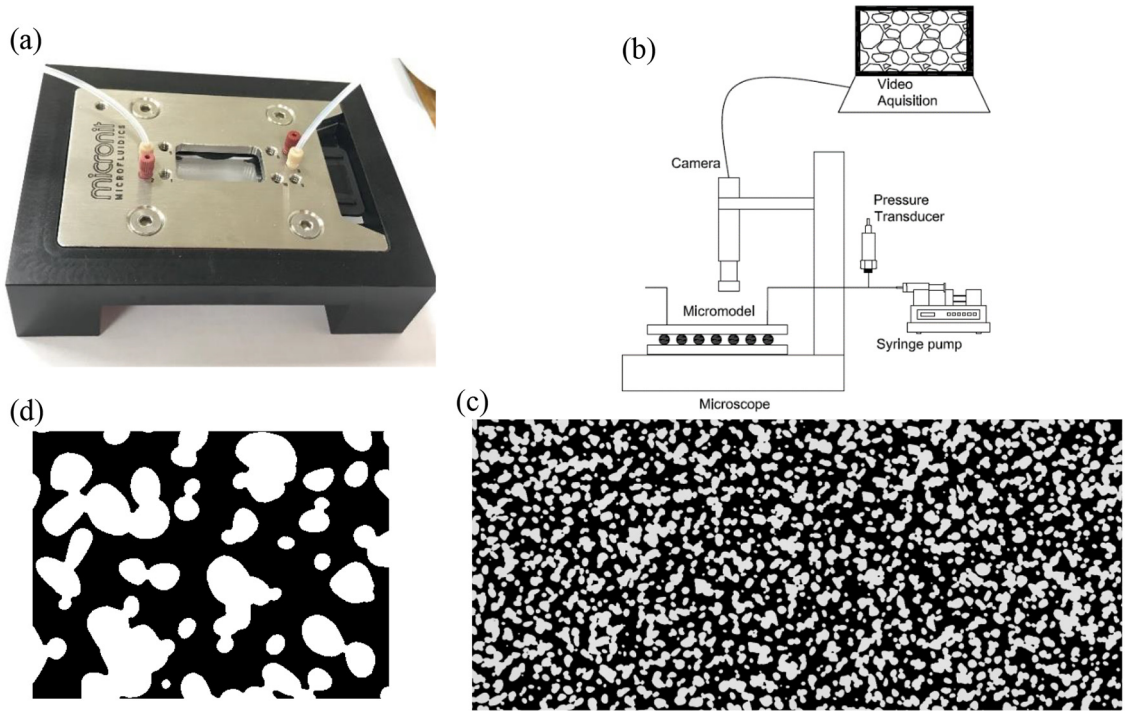

Fig. 9. (a) The micromodel holder and chip., (b) Schematic of the experimental setup, (c) Full domain geometry and (d) the imaged field of view [62].

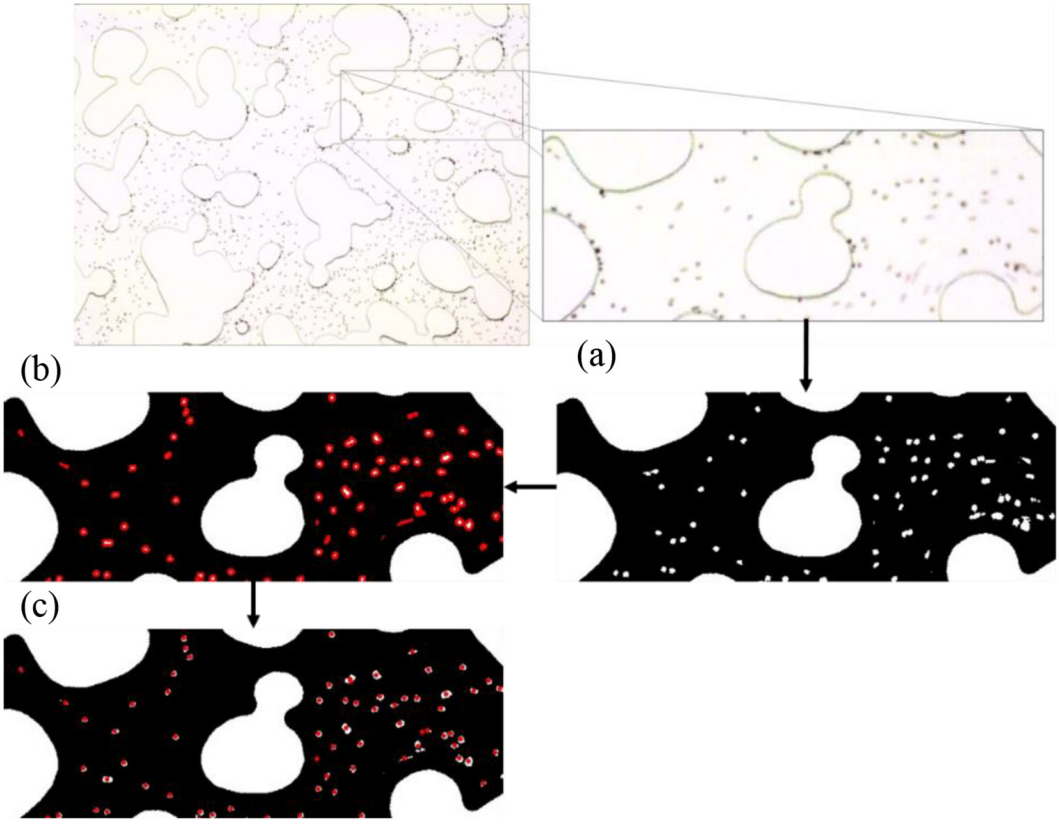

Fig. 10. Image processing workflow using OpenCV. (a) Noise reduction and binary image segmentation. (b) Extraction of contours describing the shape of each fine particle's perimeter. (c) Contours were used to calculate the centroid coordinates of each particle.

porous media. After confirming the model's setup capacity to capture single phase fluid flow behavior, the coupling of the fluid flow and particle interaction is compared to experimental results for fines migration in porous media. This was achieved by two approaches, a visual validation followed by a numerical validation. The visual validation was achieved by generating streamlines using data captured from the micromodel experiment, and CFD-DEM computed particle trajectories modelled within geometrically equivalent pore structures as shown in Fig. 14. The micromodel streamlines were generated by amalgamating the consecutive positions of the particles extracted from different frames into a single composite image. It can be noted from Fig. 14 that there is significant anecdotal match between the streamlines generated from the physical and numerical fines migration experiments.

In order to validate the coupled CFD-DEM model, velocity profiles of fine particles and their diffusion in the pore space obtained from the micromodel experiment were compared to values obtained from simulations using the same pore space geometry and initial experimental conditions. Fig. 15 shows velocities of fine particles computed from the simulation and those measured from the micromodel experiment. As can be seen in Fig. 15, a good agreement was obtained between velocity values obtained from simulations and those obtained experimentally using a micromodel of the same conditions.

Moreover, diffusion of fine particles along the x-axis and y-axis of the domain was used to provide a quantitative validation of the model by comparing the simulated results of fine migration in the pore space to the experimental measurements obtained from the micromodel experiment. Diffusion of a given particle was computed based on the standard deviation of the positions of the particle [70]. The standard deviation for displacements along a given axis of the flow domain is given as:

$$\sigma = \sqrt{\frac{\sum (x_i - \mu)^2}{N}} \tag{18}$$

Where, x_i is the i^{th} particle's position, μ is the mean position and N is the number of particles.

Fig. 16 shows values of diffusion of fine particles obtained from CFD-DEM simulations and values measured from the micromodel experiment. As can be seen from the Figure, there is a good agreement between values simulation and experiments. Moreover, an additional validation of the model's setup was conducted by comparing the percentage of fine particles retained in the pore space obtained from simulation and the micromodel experiment. To mimic experimental conditions where hydrophilic fine particles were used in the micromodel experiments, the simulated fine particles were set to have an attractive forces in the interactions with other fines and solid surfaces of the pore space in simulations. Experimentally, after a continuous injection of about 6000 particles for 20 min with a flow rate of 5 μL/min in the micromodel, approximately 42.3% of the injected particles were retained in the pore space. Comparatively, simulating the same experimental conditions, 44.1% of the injected particles were retained in the pore space.

4. Applications of the model

The CFD-DEM model described above was used to study the impact of fine particles migration on the permeability reduction of porous media. Two scenarios were simulated, namely the impact of flow velocity and size of fines on permeability reduction (i.e., pore space clogging).

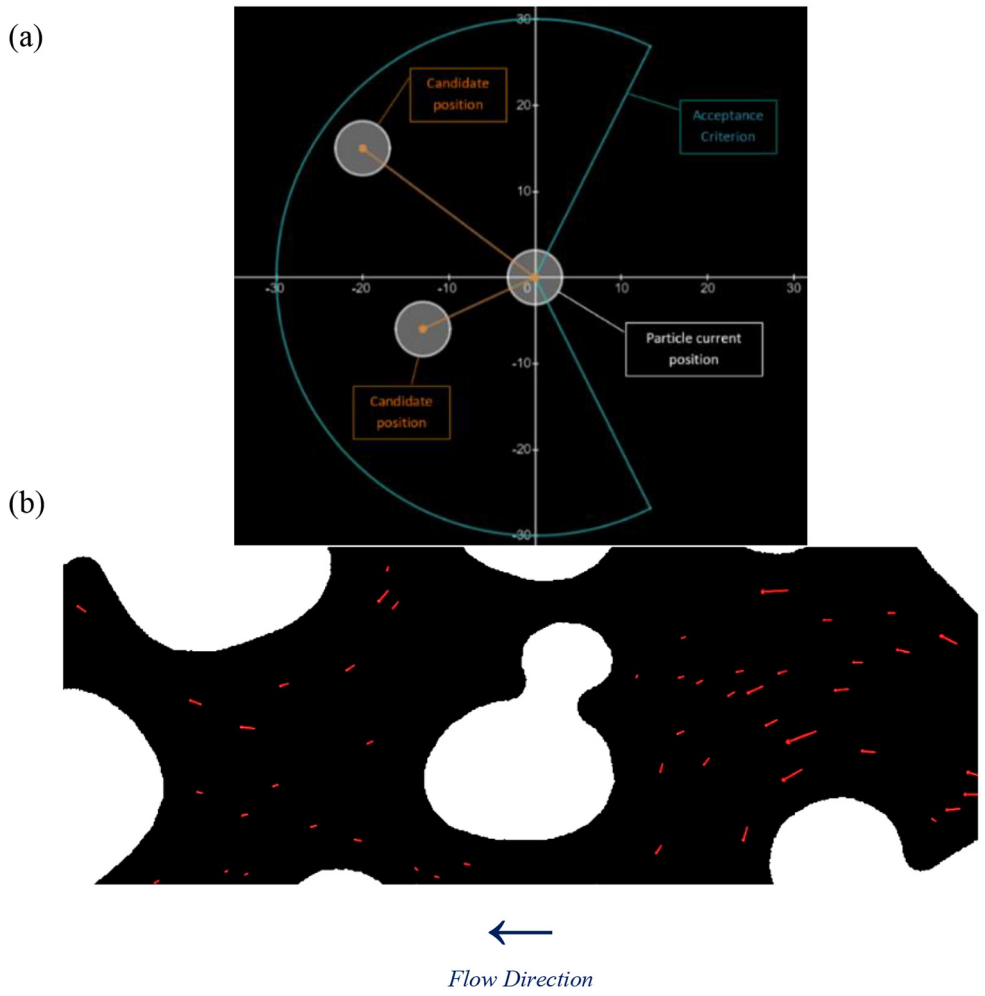

Fig. 11. (a) Resulted region and possible positions candidates for the criteria used to determine particle's position over consecutive frames. (b) Flow field estimated for two consecutive frames using the position criteria in (a).

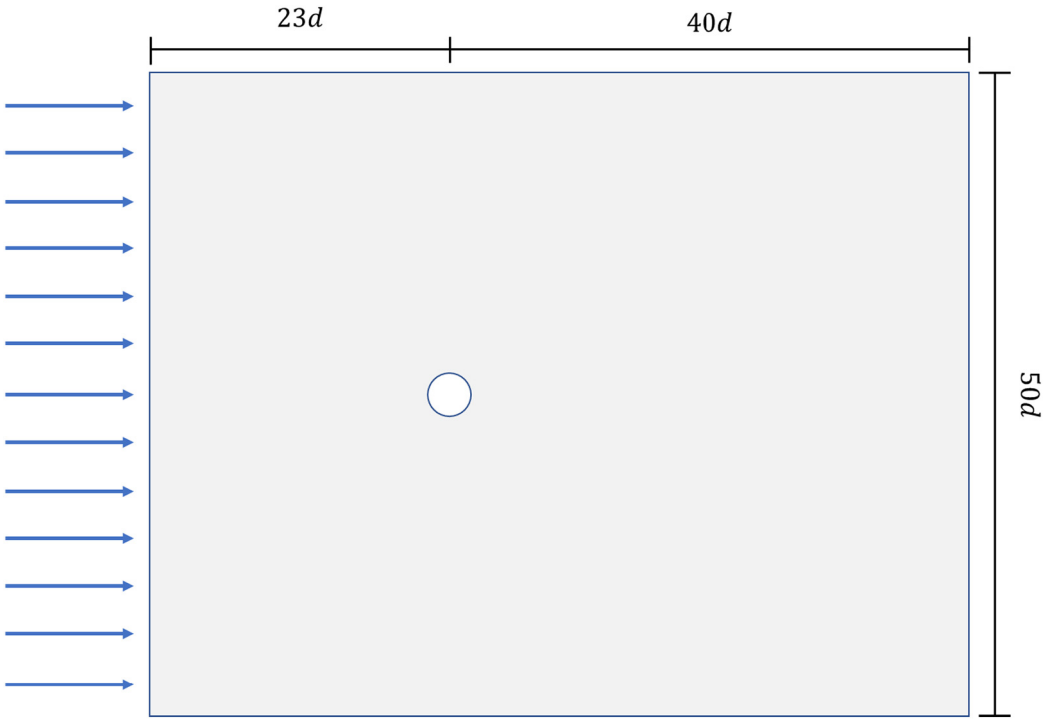

Fig. 12. Flow around cylinder fluid domain for model's setup validation.

Table 1
Fluid flow validation of the model for simple geometry.

R_e	Model Used in [66]	Model Used in [67]	Model Used in [68]	Model Used in [69]	Model Used in This Paper
10	–	2.81	2.98	2.98	2.98
20	2.2	2.04	2.06	2.16	2.13
40	1.63	1.54	1.52	1.67	1.59
100	1.4	1.39	1.3	1.32	1.38

Table 2
Microchip porosity and permeability results from the model compared to the manufacture specifications.

Parameter	Measure Values	Model Results
Permeability (Darcy)	2.5	2.65
Porosity	0.58	0.62

It is to be noted that these are just examples that illustrate the applicability of the model to investigate fines behavior in porous media. More detailed analysis will be presented in a subsequent publication.

Cross sections of the porous media used in the simulations are shown in Fig. 17. The porous media has an initial permeability of 4.17 Darcy and porosity of 0.503. The pore space has an average throat radius of 53.4 μm. Fine particles with three different sizes were used in the simulations, namely 5 μm, 10 μm and 15 μm. Five different conditions of different fine percentages and flow velocity were used in the simulations as given in Table 3.

Fig. 18 shows simulations of normalized permeability of the porous media as a function of time for different flow velocities. As can be seen from the simulations, permeability reduction due to fine migration in porous media is directly proportional to the flow velocity. For flow velocity of 0.024 *cm/min*, a reduction of 3.2% of permeability was observed. However, increasing the flow velocity to 0.048 *cm/min* resulted in a 5.9% reduction in the permeability whereas increasing the velocity to 0.24 *cm/min* caused a 23.2% drop in permeability. These findings are in agreement with previous micromodel experiments where fine particles of density of 1 g/cm^3 were used in the experiments [71]. It was also observed, in Fig. 18, that the time needed to attain the critical fine content required to induce clogging and permeability reduction within pore space is directly proportional to the flow velocity. As can be seen from Fig. 18, the time required to develop bridging and subsequent clogging of the pore space that lead to permeability reduction decreases as the flow velocity increases. For instance, at high flow velocity (i.e, 0.24 *cm/ min*),a rapid bridging and clogging of porous media was developed as opposed to slow initial bridging at smaller velocities. This observation and trend is consistent with what was observed in previous studies where computed tomography [4] and micromodel experiments [72] were conducted to investigate clogging behavior of porous media. The rapid bridging and clogging at higher velocity is mainly attributed to the increased capturing efficiency [71] and to the high energy gained by particles which in turn accelerates their deposition [74].

Fig. 19 shows the impact of sizes of fine particles on permeability reduction of the porous media for a given flow velocity (i.e., 0.24 *cm/* min). Three different sizes of fines were considered in the simulations, namely 5 μm, 10 μm, and a polydisperse suspension of 5, 10 and 15 μm. As can be seen in Fig. 19, the size of the fine particles has a significant impact on permeability reduction. A similar pattern of continuous decrease in permeability was observed in all cases where the reduction in permeability increased as the size of particles increased. The 5 μm fine particles caused a 20% reduction in the permeability whereas a 22.5% reduction of permeability was observed in case of 10 μm particles flow. This can be explained by relating the size of particles to their transport behavior, larger particles travel along the stream of flow which provides a greater tendency of deposition on grain surfaces whereas the tendency of particles dispersion increases as the size of particles decreases [75]. Moreover, large particles tend to clog small pore throats in the pore space which causes a profound reduction in the permeability [29,76]. A faster and larger reduction in permeability was observed when a suspension of polydisperse particles was injected where a reduction of 23.2% was attained. These observations are consistent with previous studies that investigated the clogging and bridging behavior due to fines flow [73,77]. Moreover, it was observed that the time required to attain a noticeable permeability reduction depends on the size of injected particles. A suspension of polydisperse particles led to a faster reduction in permeability as opposed to a monodisperse suspension. These observations are in agreement with previous studies where it was observed that large particles tend to induce throat-clogging which lead to a relatively faster permeability reduction as compared to small particles that develop clogging due to sequential deposition of particles [78–80].

5. Conclusions

Having application towards numerous fields within the physical sciences and engineering, the development of modelling frameworks capable of representing fines migration at the pore-scale within heterogeneous porous media presents significant conceptual and technical challenges. Though several such frameworks have been presented in the literature [29–33], previous work provided minimal model validation. Specifically, these works were unable to provide physical validation that their models were capable of capturing the bulk transport dynamics of fine suspensions within complex pore networks via robust comparison with an equivalent system. The IBM coupled CFD-DEM parallel model presented herein is capable of representing both fluid-fluid

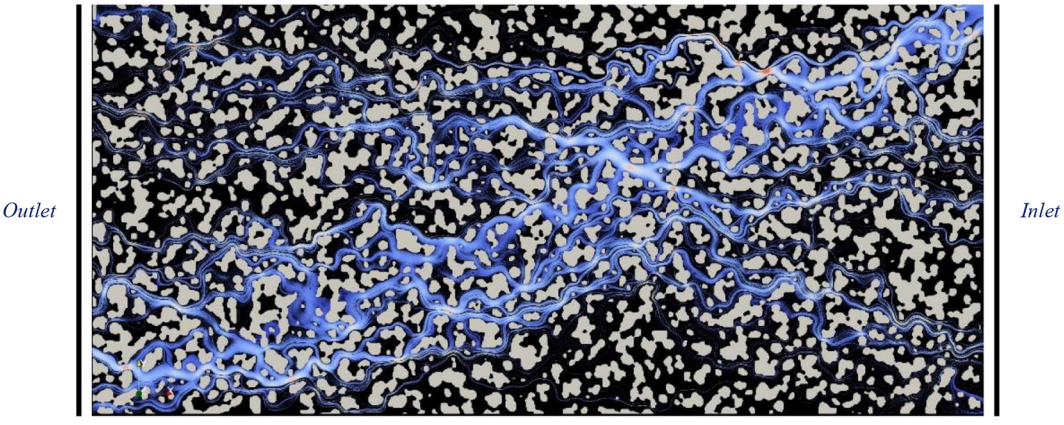

Fig. 13. Flow in the microfluidic chip used to validate the model setup.

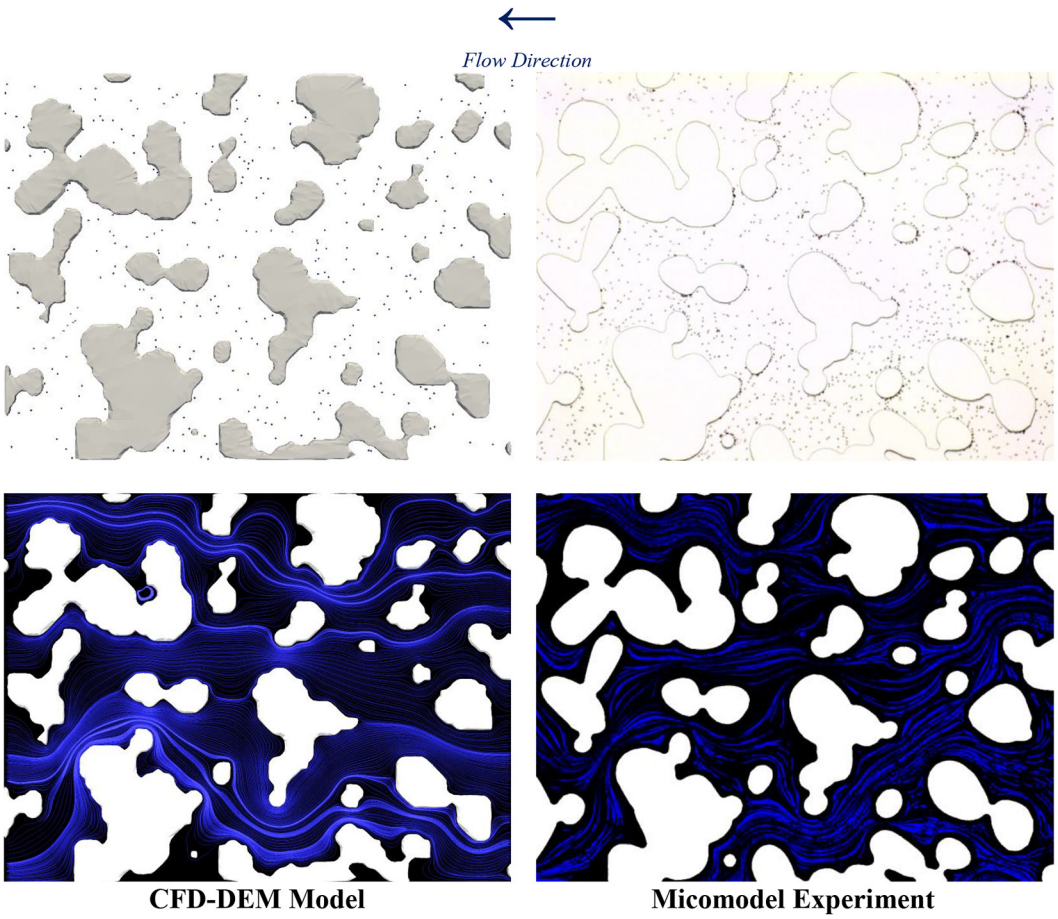

Fig. 14. Comparison between flow streamlines produced by the numerical simulation and micromodel experiment.

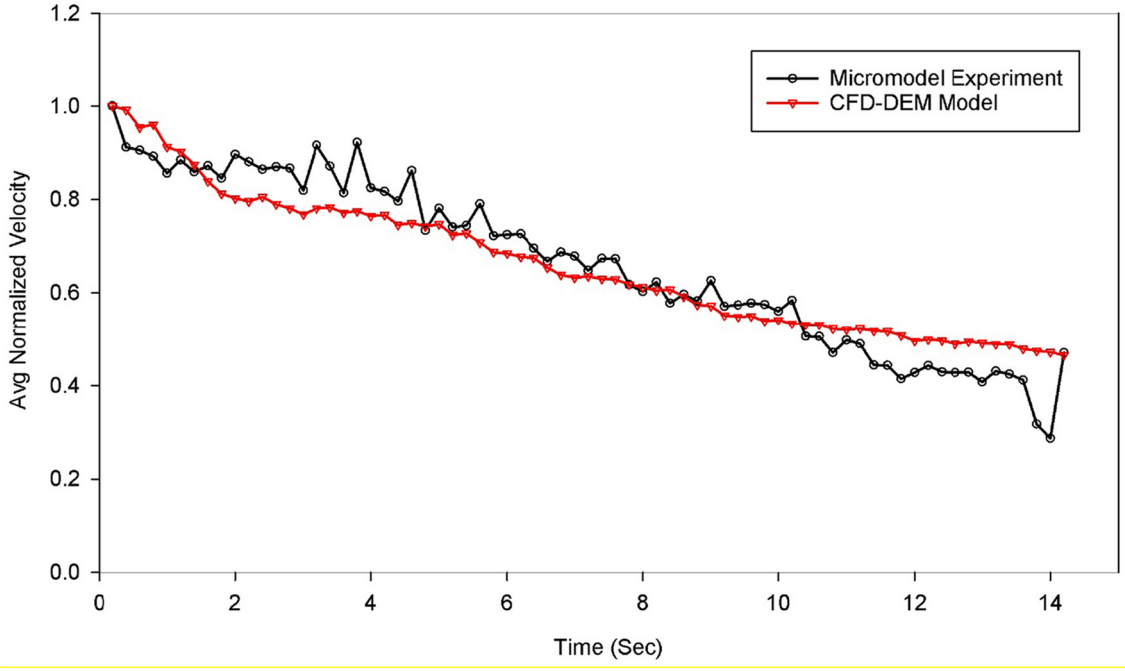

Fig. 15. Average velocity of particles obtained from numerical and physical micromodel experiment.

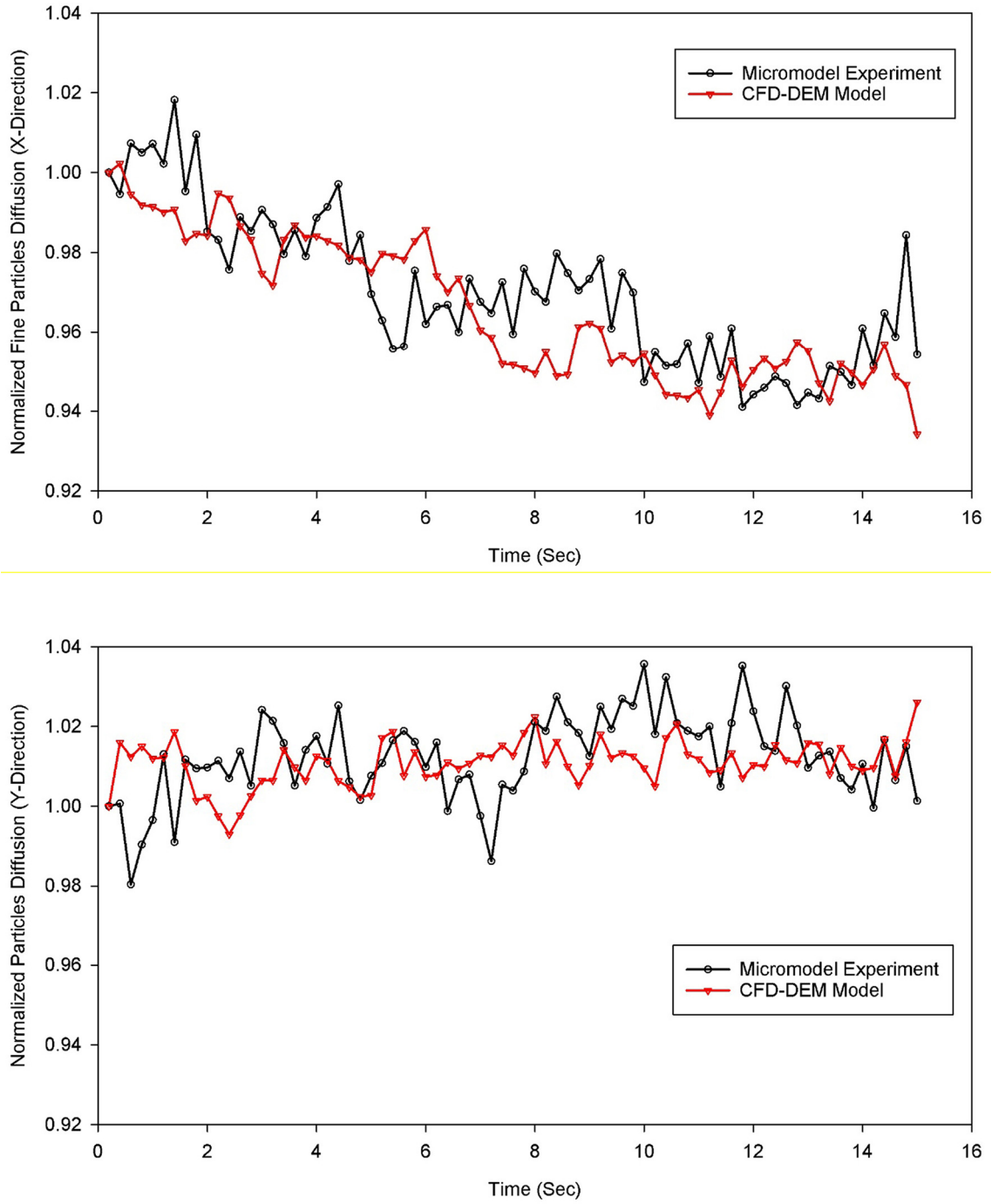

Fig. 16. Comparison between the diffusion of fine particles in the numerical simulation and physical micromodel experiments used to validate the model setup.

and fluid-solid interactions and is capable of handling several hundred to several thousand mobile particles simultaneously within the modelling domain. The presented framework was shown to capture the bulk dynamics of fine particulate transport and deposition within geologically realistic, complex flow domains consisting of tens of connected pore bodies, as demonstrated by comparison with microfluidic experiments through equivalent geometries.

The model was used to study the impact of flow velocity and size of fines on permeability reduction of porous media due to migration of fine particles. Simulations indicate that permeability reduction due to fine migration in porous media is directly proportional to flow velocity. For flow velocity of 0.024 *cm/min*, a reduction of 3.2% of permeability was observed. However, increasing the flow velocity to 0.048 *cm/min* resulted in a 5.9% reduction in the permeability whereas increasing the velocity to 0.24 *cm/min* caused a 23.2% drop in permeability. The time required to develop bridging and subsequent clogging of the pore space that lead to permeability reduction decreases as the flow velocity increases. The size of the fine particles has a significant impact on permeability reduction where the reduction in permeability increases as the size of particles increases. A faster and larger reduction in permeability was observed when a suspension of polydisperse particles was injected as opposed to a monodisperse suspension.

Several adaptations can be made to the presented CFD-DEM framework to enhance functionality and expand the potential application pool.

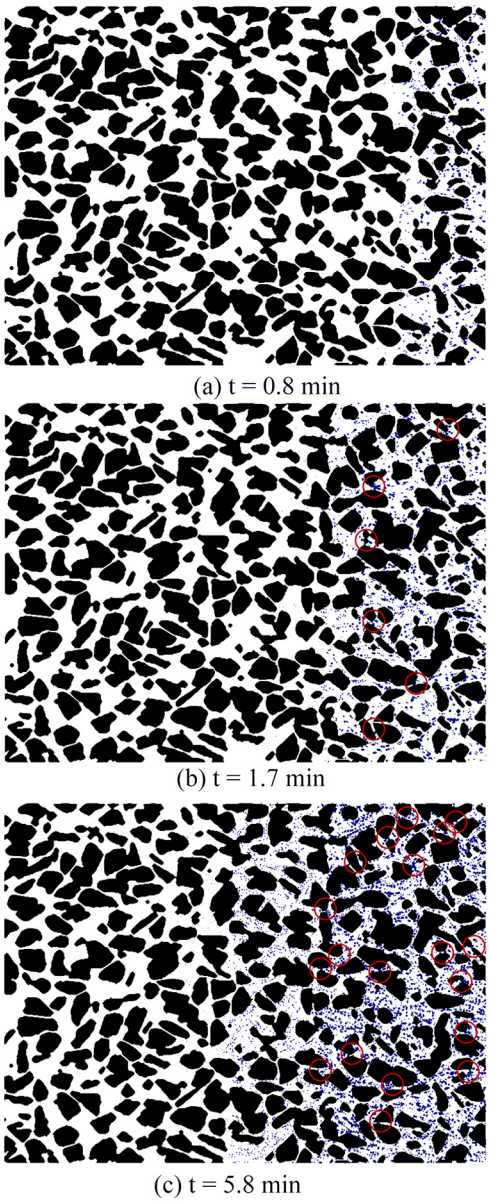

Fig. 17. Application of the model: distribution of fine particles inside the porous media at velocity of 0.42 cm/min at different times (a) t = 0.8 min, (b) t = 1.7 min and (c) at t = 5.8 min.

Future modifications could include using more realistic three-dimensional geometries to provide greater equivalence towards real geological and synthetic pore systems. Furthermore, the electrostatic charges of the particles could be included to capture forces such as DLVO interactions, which have been ignored within the present framework. Finally, the modelling framework could include (rigidly) deformable finite volume meshes, generated a priori to encompass fluid solid interactions with the framework grains. Such an adaptation would permit the representation of dynamic channelization and preferential transport and deposition of fine particulate observed within unconfined substrates, as previously observed

Table 3
Flow velocity and fine particles size distributions used in the permeability reduction simulation cases.

Simulation Case	Flow Velocity (cm/min)	Fine Particles Insertion Percentage		
		5 μm	10 μm	15 μm
I	0.024	0.25	0.5	0.25
II	0.048	0.25	0.5	0.25
III	0.24	0.25	0.5	0.25
IV	0.024	1	0	0
V	0.024	0	1	0

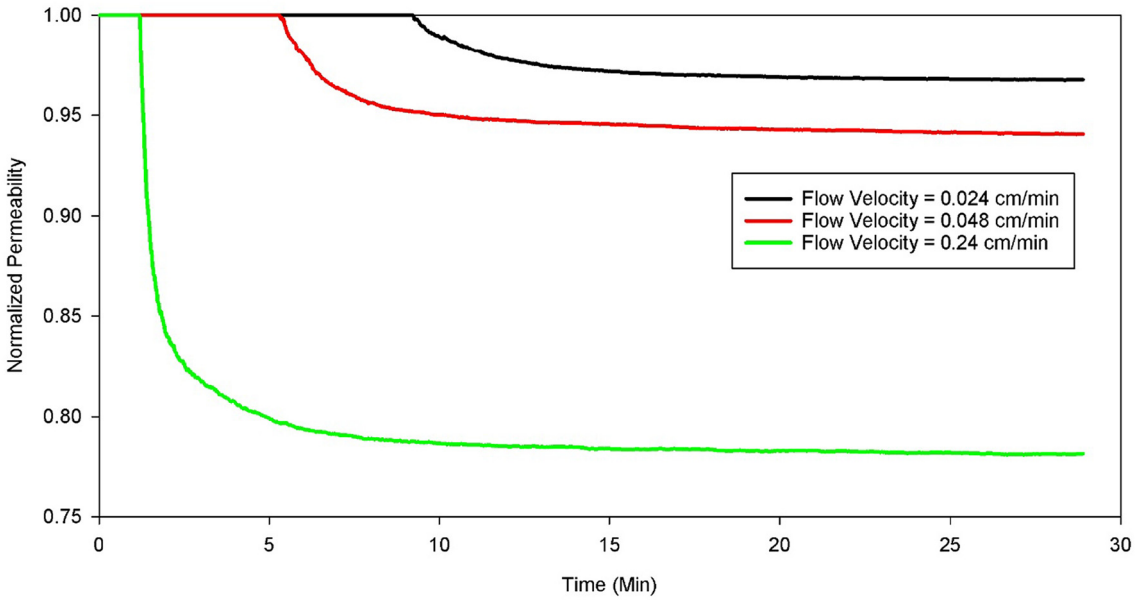

Fig. 18. Application of the model: the impact of the flow velocity on permeability reduction of porous media (i.e., pore space clogging) due to fine migration.

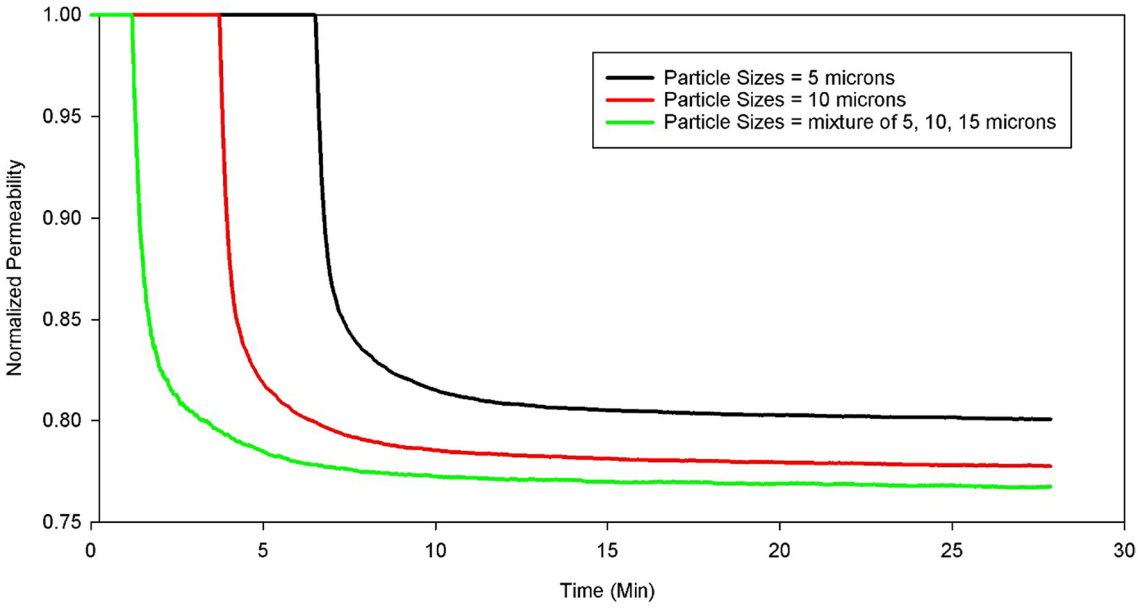

Fig. 19. Application of the model: The impact of the size of fines on permeability reduction of porous media due to fine migration. Simulation of different fine sizes at flow velocity of 0.24 cm/min.

in in-situ experimental core flood experiments imaged using synchrotron x-ray microcomputed tomography [4].

Declaration of Competing Interest

The authors declare that they have no known competing financial interests or personal relationships that could have appeared to influence the work reported in this paper.

Acknowledgment

Open Access funding provided by the Qatar National Library. This publication was made possible by funding from NPRP grant #NPRP8-594-2-244 from the Qatar National Research Fund (a member of Qatar Foundation). Any opinions, findings, and conclusions or recommendations expressed in this paper are those of the authors and do not necessarily reflect the view of funding agencies.

References

[1] C.K. Kartic, F.H. Scott, Migrations of Fines in Porous Media, Kluwer Academic Publishers, 1998.
[2] S.C. Cao, J. Jang, J. Jung, W.F. Waite, T.S. Collett, P. Kumar, 2D micromodel study of clogging behavior of fine-grained particles associated with gas hydrate production in NGHP-02 gas hydrate reservoir sediments, Mar. Pet. Geol. (2018) https://doi.org/10.1016/j.marpetgeo.2018.09.010.
[3] J. Jang, S.C. Cao, L.A. Stern, J. Jung, W.F. Waite, Impact of pore fluid chemistry on fine-grained sediment fabric and compressibility, J. Geophys. Res. Solid Earth 0 (2018) 5495–5514, https://doi.org/10.1029/2018JB015872%0A.

[4] Z.A. Jarrar, R.I. Al-Raoush, J.A. Hannun, K.A. Alshibli, J. Jung, 3D synchrotron computed tomography study on the influence of fines on gas driven fractures in sandy sediments, Geomech. Energy Environ. 23 (2018) 1–10, https://doi.org/10.1016/j.gete.2018.11.001.

[5] L. Chequer, P. Bedrikovetsky, Suspension-colloidal flow accompanied by detachment of oversaturated and undersaturated fines in porous media, Chem. Eng. Sci. 198 (2019) 16–32, https://doi.org/10.1016/j.ces.2018.12.033.

[6] G. Han, T.H. Kwon, J.Y. Lee, J. Jung, Fines migration and pore clogging induced by single- and two-phase fluid flows in porous media: From the perspectives of particle detachment and particle-level forces, Geomech. Energy Environ. 23 (2019), 100131, https://doi.org/10.1016/j.gete.2019.100131.

[7] M.M. Sharma, Y.C. Yortsos, Permeability Impairment Due to Fines Migration in Sandstones, 1986. https://doi.org/10.2118/14819-MS.

[8] T.D. Seers, N. Alyafei, Open Source Toolkit for Micro-Model Generation Using 3D Printing, 2018. https://doi.org/10.2118/190852-MS.

[9] K.C. Khilar, H.S. Fogler, Water sensitivity of sandstones, Soc. Pet. Eng. J. 23 (1983) 55–64, https://doi.org/10.2118/10103-PA.

[10] R.N. Valdya, H.S. Fogler, Fines migration and formation damage: influence of pH and ion exchange, SPE Prod. Eng. 7 (1992) 325–330, https://doi.org/10.2118/19413-PA.

[11] S.A. Shedid, M.A. Saad, Comparison and sensitivity analysis of water saturation models in shaly sandstone reservoirs using well logging data, J. Pet. Sci. Eng. 156 (2017) 536–545, https://doi.org/10.1016/j.petrol.2017.06.005.

[12] X. Li, W. Zhang, Y. Qin, T. Ma, J. Zhou, S. Du, Fe–colloid cotransport through saturated porous media under different hydrochemical and hydrodynamic conditions, Sci. Total Environ. 647 (2019) 494–506, https://doi.org/10.1016/j.scitotenv.2018.08.010.

[13] L. Zhao, H. Jiang, J. Li, J. Li, Pore-scale evaluation on the mechanism of water sensitivity for sandstones containing non-swelling clays, Arab. J. Geosci. 13 (2020) 54, https://doi.org/10.1007/s12517-019-5023-7.

[14] J.W. Jung, J. Jang, J.C. Santamarina, C. Tsouris, T.J. Phelps, C.J. Rawn, Gas production from hydrate-bearing sediments: The role of fine particles, Energy Fuel 26 (2012) 480–487, https://doi.org/10.1021/ef101651b.

[15] S. Uchida, J. Lin, E.M. Myshakin, Y. Seol, T.S. Collett, R. Boswell, Numerical Simulations of Sand Production in Interbedded Hydrate-Bearing Sediments during Depressurization, 9th Int. Conf. Gas Hydrates, 2017.

[16] W.F. Waite, J. Jang, T.S. Collett, P. Kumar, L.W. Chatrou, M.P. Escribano, M.A. Viruel, J.W. Maas, E. James, J.I. Hormaza, Downhole physical property-based description of a gas hydrate petroleum system in NGHP-02 Area C_ A channel, levee, fan complex in the Krishna-Godavari Basin offshore eastern India, Mar. Pet. Geol. (2018) https://doi.org/10.1016/j.ympev.2009.07.024.

[17] X. Shi, M. Prodanović, J. Holder, K.E. Gray, D. DiCarlo, Coupled solid and fluid mechanics modeling of formation damage near wellbore, J. Pet. Sci. Eng. 112 (2013) 88–96, https://doi.org/10.1016/j.petrol.2013.10.011.

[18] R.N. Vaidya, H.S. Fogler, Formation damage due to colloidally induced fines migration, Colloids Surf. A Physicochem. Eng. Asp. 50 (1990) 215–229, https://doi.org/10.1016/0166-6622(90)80265-6.

[19] K.S. Richards, K.R. Reddy, Critical appraisal of piping phenomena in earth dams, Bull. Eng. Geol. Environ. 66 (2007) 381–402, https://doi.org/10.1007/s10064-007-0095-0.

[20] C.D. Nguyen, N. Benahmed, P. Philippe, E.V. Diaz Gonzalez, Experimental study of erosion by suffusion at the micro-macro scale, EPJ Web Conf. 140 (2017) 09024, https://doi.org/10.1051/epjconf/201714009024.

[21] X. Lei, Z. Yang, S. He, E. Liu, H. Wong, X. Li, Hydro-mechanical analysis of rainfall-induced fines migration process within unsaturated soils, J. Mt. Sci. 14 (2017) 2603–2619, https://doi.org/10.1007/s11629-017-4359-2.

[22] Y. Cui, Y. Yin, C. Guo, in: Ž. Arbanas, P.T. Bobrowsky, K. Konagai, K. Sassa, K. Takara (Eds.), Investigation of Internal Erosion of Wide Grading Loose Soil—A Micromechanics-Based Study BT - Understanding and Reducing Landslide Disaster Risk: Volume 6 Specific Topics in Landslide Science and Applications, Springer International Publishing, Cham 2021, pp. 155–161, https://doi.org/10.1007/978-3-030-60713-5_16.

[23] M.Y. Corapcioglu, S. Jiang, Colloid-facilitated groundwater contaminant transport, Water Resour. Res. 29 (1993) 2215–2226, https://doi.org/10.1029/93WR00404.

[24] F.H. Frimmel, F. von der Kammer, H.-C. Flemming, Colloidal Transport in Porous Media, 2007.

[25] L.W. de Jonge, C. Kjaergaard, P. Moldrup, Colloids and colloid-facilitated transport of contaminants in soils, Vadose Zo. J. 3 (2010) 321, https://doi.org/10.2136/vzj2004.0321.

[26] S. Datta, S. Redner, Gradient clogging in depth filtration, Phys. Rev. E 58 (1998) R1203.

[27] M. Rodgers, J. Mulqueen, M.G. Healy, Surface clogging in an intermittent stratified sand filter, Soil Sci. Soc. Am. J. 68 (2010) 1827, https://doi.org/10.2136/sssaj2004.1827.

[28] J.L. Sherard, L.P. Dunnigan, J.R. Talbot, Basic properties of sand and gravel filters, in, Geotech. Spec. Publ. (2002) 1941–1957, https://doi.org/10.1061/(ASCE)0733-9410(1984)110:6(684).

[29] S. Hirabayashi, T. Sato, K. Mitsuhori, Y. Yamamoto, Microscopic numerical simulations of suspension with particle accumulation in porous media, Powder Technol. 225 (2012) 143–148, https://doi.org/10.1016/j.powtec.2012.04.001.

[30] G. Boccardo, D.L. Marchisio, R. Sethi, Microscale simulation of particle deposition in porous media, J. Colloid Interface Sci. 417 (2014) 227–237, https://doi.org/10.1016/j.jcis.2013.11.007.

[31] Q. Li, V. Prigiobbe, Numerical simulations of the migration of fine particles through porous media, Transp. Porous Media 122 (2018) 745–759, https://doi.org/10.1007/s11242-018-1024-3.

[32] K. Zhou, J. Hou, Q. Sun, L. Guo, S. Bing, Q. Du, C. Yao, A study on particle suspension flow and permeability impairment in porous media using LBM–DEM–IMB simulation method, Transp. Porous Media 124 (2018) 681–698, https://doi.org/10.1007/s11242-018-1089-z.

[33] J. Su, G. Chai, L. Wang, W. Cao, Z. Gu, C. Chen, X.Y. Xu, Pore-scale direct numerical simulation of particle transport in porous media, Chem. Eng. Sci. 74 (2019) 613–627, https://doi.org/10.1016/j.ces.2019.01.033.

[34] H. Lomax, T. Pulliam, D. Zingg, T. Kowalewski, Fundamentals of computational fluid dynamics, Appl. Mech. Rev. (2002)https://doi.org/10.1115/1.1483340.

[35] J. Boudet, Finite volume methods, Theor. Comput. Fluid Dyn. (2011) 1–24, https://doi.org/10.1201/b11033-2.

[36] H.G. Weller, G. Tabor, H. Jasak, C. Fureby, A tensorial approach to computational continuum mechanics using object-oriented techniques, Comput. Phys. 12 (1998) 620–631, https://doi.org/10.1063/1.168744.

[37] A. Goniva, C. Kloss, N.G. Deen, J.A.M. Kuipers, S. Pirker, Influence of rolling friction on single spout fluidized bed simulation, Particuology. 10 (2012) 582–591, https://doi.org/10.1016/j.partic.2012.05.002.

[38] N.V. Brilliantov, F. Spahn, J.-M. Hertzsch, T. Pöschel, Model for collisions in granular gases, Phys. Rev. E 53 (1996) 5382–5392, https://doi.org/10.1103/PhysRevE.53.5382.

[39] L.E. Silbert, D. Erta, G.S. Grest, T.C. Halsey, D. Levine, S.J. Plimpton, Granular flow down an inclined plane: Bagnold scaling and rheology, Phys. Rev. E 64 (2001) 51302, https://doi.org/10.1103/PhysRevE.64.051302.

[40] A. Di Renzo, F.P. Di Maio, An improved integral non-linear model for the contact of particles in distinct element simulations, Chem. Eng. Sci. 60 (2005) 1303–1312, https://doi.org/10.1016/j.ces.2004.10.004.

[41] H.P. Zhang, H.A. Makse, Jamming transition in emulsions and granular materials, Phys. Rev. E 72 (2005) 11301, https://doi.org/10.1103/PhysRevE.72.011301.

[42] T. Schwager, T. Pöschel, Coefficient of restitution and linear–dashpot model revisited, Granul. Matter 9 (2007) 465–469, https://doi.org/10.1007/s10035-007-0065-z.

[43] J. Ai, J.-F. Chen, J.M. Rotter, J.Y. Ooi, Assessment of rolling resistance models in discrete element simulations, Powder Technol. 206 (2011) 269–282, https://doi.org/10.1016/j.powtec.2010.09.030.

[44] Z. Zhou, S. Kuang, K. Chu, A. Yu, Discrete particle simulation of particle–fluid flow: model formulations and their applicability, J. Fluid Mech. 661 (2010) 482–510, https://doi.org/10.1017/S002211201000306X.

[45] A.A. Shirgaonkar, M.A. MacIver, N.A. Patankar, A new mathematical formulation and fast algorithm for fully resolved simulation of self-propulsion, J. Comput. Phys. 228 (2009) 2366–2390, https://doi.org/10.1016/j.jcp.2008.12.006.

[46] A. Agesen, L. Blæsbjerg, A. Ehlers, Particle Accumulation in Square Duct Cavity with Laminar Flow, 2019.

[47] R.I. Issa, A.D. Gosman, A.P. Watkins, The computation of compressible and incompressible recirculating flows by a non-iterative implicit scheme, J. Comput. Phys. 62 (1986) 66–82, https://doi.org/10.1016/0021-9991(86)90100-2.

[48] R.I. Issa, Solution of the implicitly discretised fluid flow equations by operator-splitting, J. Comput. Phys. 62 (1986) 40–65, https://doi.org/10.1016/0021-9991(86)90099-9.

[49] R.I.I. Paulo, J. Oliveira, An Improved Piso Algorithm for the Computation of Buoyancy-Driven Flows, Numer. Heat Transf. Part B Fundam. 40 (2001) 473–493, https://doi.org/10.1080/104077901753306601.

[50] J.H. Ferziger, M. Perić, Computational Methods for Fluid Dynamics, Springer, Berlin, Heidelberg, 2002. https://doi.org/10.1017/CBO9781107415324.004.

[51] H.A. van der Vorst, Bi-CGSTAB: A fast and smoothly converging variant of Bi-CG for the solution of nonsymmetric linear systems, SIAM J. Sci. Stat. Comput. (1992) https://doi.org/10.1137/0913035.

[52] R. Barrett, M. Berry, T.F. Chan, J. Demmel, J. Donato, J. Dongarra, V. Eijkhout, R. Pozo, C. Romine, H. Van der Vorst, Templates for the Solution of Linear Systems: Building Blocks for Iterative Methods, 2nd edition SIAM, Philadelphia, PA, 1994.

[53] T. Behrens, OpenFOAM's Basic Solvers for Linear Systems of Equations, Report, 18, 2009.

[54] C.S. Peskin, Flow patterns around heart valves: A numerical method, J. Comput. Phys. 10 (1972) 252–271, https://doi.org/10.1016/0021-9991(72)90065-4.

[55] H. Bandringa, Immersed Boundary Methods, 2010. https://doi.org/10.1002/fld.1077.

[56] J. Tu, G.-H. Yeoh, C. Liu, Chapter 9 - Some advanced topics in CFD, in: J. Tu, G.-H. Yeoh, C. Liu (Eds.), Comput. Fluid Dyn, Third ed.Butterworth-Heinemann 2018, pp. 369–417, https://doi.org/10.1016/B978-0-08-101127-0.00009-X.

[57] G. Tryggvason, Chapter 6 - Computational fluid dynamics, in: P.K. Kundu, I.M. Cohen, D.R. Dowling (Eds.), Fluid Mech, Sixth ed.Academic Press, Boston 2016, pp. 227–291, https://doi.org/10.1016/B978-0-12-405935-1.00006-X.

[58] C. Goniva, C. Kloss, A. Hager, G. Wierink, S. Pirker, A multi-purpose open source CFD-DEM approach, 8th Int. Conf. CFD Oil Gas, Metall. Process Ind. Trondheim, Norw. 21-23 June 2011, 2011.

[59] A. Hager, C. Kloss, S. Pirker, C. Goniva, Parallel resolved open source CFD-DEM: method, validation and application, J. Comput. Multiph. Flows. 6 (2014) 13–27, https://doi.org/10.1260/1757-482X.6.1.13.

[60] H. Norouzi, R. Zarghami, R. Sotudeh-Gharebagh, N. Mostoufi, DEM formulation, Coupled CFD-DEM Model, John Wiley & Sons, Ltd 2016, pp. 15–67, https://doi.org/10.1002/9781119005315.ch2.

[61] S. Nishad, R.I. Al-Raoush, M.Y.D. Alazaiza, Release of colloids in saturated porous media under transient hydro-chemical conditions: A pore-scale study, Colloids Surf. A Physicochem. Eng. Asp. 614 (2021) 126188. https://doi.org/10.1016/j.colsurfa.2021.126188.

[62] S. Nishad, R.I. Al-Raoush, Colloid retention and mobilization mechanisms under different physicochemical conditions in porous media: A micromodel study, Powder Technol. 377 (2021) 163–173, https://doi.org/10.1016/j.powtec.2020.08.086.

[63] G. Bradski, The OpenCV Library, Dr. Dobb's J. Softw. Tools, 2000.

[64] R. Szeliski, Computer Vision Algorithms and Applications, 2011.

[65] S. Nishad, R.I. Al-Raoush, Impact of Ionic Strength on Colloid Retention in a Porous Media: A Micromodel Study, 2020 715–723, https://doi.org/10.29117/cic.2020.0092.
[66] S.-W. Su, M.-C. Lai, C.-A. Lin, An immersed boundary technique for simulating complex flows with rigid boundary, Comput. Fluids 36 (2007) 313–324, https://doi.org/10.1016/j.compfluid.2005.09.004.
[67] A.L.F. Lima e Silva, A. Silveira-Neto, J.J.R. Damasceno, Numerical simulation of two-dimensional flows over a circular cylinder using the immersed boundary method, J. Comput. Phys. 189 (2003) 351–370, https://doi.org/10.1016/S0021-9991(03)00214-6.
[68] J. Deng, X.-M. Shao, A.-L. Ren, A new modification of the immersed-boundary method for simulating flows with complex moving boundaries, Int. J. Numer. Methods Fluids 52 (2006) 1195–1213, https://doi.org/10.1002/fld.1237.
[69] R. Maniyeri, Numerical study of flow over a cylinder using an immersed boundary finite volume method, Int. J. Eng. Res. 3 (2014) 213–216, https://doi.org/10.17950/ijer/v3s4/406.
[70] D.A. Chin, Water-Quality Engineering in Natural Systems, 2006https://doi.org/10.1002/0471784559.
[71] Q. Liu, B. Zhao, J.C. Santamarina, Particle migration and clogging in porous media: a convergent flow microfluidics study, J. Geophys. Res. Solid Earth 124 (2019) 9495–9504, https://doi.org/10.1029/2019JB017813.
[72] G.C. Agbangla, É. Climent, P. Bacchin, Experimental investigation of pore clogging by microparticles: Evidence for a critical flux density of particle yielding arches and deposits, Sep. Purif. Technol. 101 (2012) 42–48, https://doi.org/10.1016/j.seppur.2012.09.011.
[73] Z. Chen, Y. Li, Y. Xie, X. Wang, In-situ particle migration and plugging mechanism in unconsolidated sandstone and sanding management, Chem. Technol. Fuels Oils 53 (2017) 759–767, https://doi.org/10.1007/s10553-017-0858-7.
[74] Z.B. Sendekie, P. Bacchin, Colloidal jamming dynamics in microchannel bottlenecks, Langmuir. 32 (2016) 1478–1488, https://doi.org/10.1021/acs.langmuir.5b04218.
[75] M. Auset, A.A. Keller, Pore-scale processes that control dispersion of colloids in saturated porous media, Water Resour. Res. 40 (2004) https://doi.org/10.1029/2003WR002800.
[76] Q. Liu, B. Zhao, J.C. Santamarina, Particle migration and clogging in porous media: a convergent flow microfluidics study, J. Geophys. Res. Solid Earth (2019) 1–10, https://doi.org/10.1029/2019jb017813.
[77] H.J. Khan, M.S. Mirabolghasemi, H. Yang, M. Prodanović, D.A. DiCarlo, M.T. Balhoff, Study of formation damage caused by retention of bi-dispersed particles using combined pore-scale simulations and particle flooding experiments, J. Pet. Sci. Eng. 158 (2017) 293–308, https://doi.org/10.1016/j.petrol.2017.08.061.
[78] A. Sauret, E.C. Barney, A. Perro, E. Villermaux, H.A. Stone, E. Dressaire, Clogging by sieving in microchannels: Application to the detection of contaminants in colloidal suspensions, Appl. Phys. Lett. 105 (2014) https://doi.org/10.1063/1.4893459.
[79] B. Mustin, B. Stoeber, Deposition of particles from polydisperse suspensions in microfluidic systems, Microfluid. Nanofluid. 9 (2010) 905–913, https://doi.org/10.1007/s10404-010-0613-4.
[80] L. Isa, R. Besseling, A.N. Morozov, W.C.K. Poon, Velocity oscillations in microfluidic flows of concentrated colloidal suspensions, Phys. Rev. Lett. 102 (2009) 1–4, https://doi.org/10.1103/PhysRevLett.102.058302.